

Over 98% Efficiency SiC-MOSFET Based Four-Phase Interleaved Bidirectional DC–DC Converter Featuring Wide-Range Voltage Ratio

Shiqiang Liu ¹, Student Member, IEEE, Guiyi Dong ¹, Student Member, IEEE, Tomokazu Mishima ², Senior Member, IEEE, and Ching-Ming Lai ³, Senior Member, IEEE

Abstract—A novel floating four-phase interleaved charge-pump bidirectional dc–dc converter (F4P-ICPBDC) with wide buck/boost voltage ratio is proposed in this article. The interleaved structure is employed to mitigate the current ripple across the low-voltage side capacitor and inductors, while the floating configuration facilitates the high buck/boost voltage conversion ratio. To ensure a balanced average inductor current throughout the entire range of duty cycle, a cost-effective asymmetric duty limit control strategy is implemented. In addition, bidirectional synchronous rectification operations are seamlessly carried out without the need for additional hardware, thereby enhancing the overall converter efficiency. Furthermore, the full operating principles, device stresses, current ripple characteristics, as well as parameters design guideline of the converter are illustrated. Finally, A 1 kW-50 kHz prototype, utilizing SiC-MOSFETs, is developed to validate the wide buck/boost voltage ratio of the proposed converter between the constant low-voltage side (72 V) and the adjustable high-voltage side (400–800 V). The maximum efficiencies of the converter are recorded as 98.3% in the Buck mode and 97.6% in the Boost mode, respectively. Experimental results validate the feasibility and the efficacy of the proposed converter.

Index Terms—Asymmetrical duty limit control (A-DLC), bidirectional dc–dc converter, charge-pump, floating interleaved topology, synchronous rectification (SR), wide buck/boost voltage ratio.

I. INTRODUCTION

NOWADAYS, the escalating issue of greenhouse gas emissions, a significant factor to climate change, has emerged as a formidable challenge. To mitigate this issue, one solution being promoted is the use of electric vehicles (EVs) [1], which are

Manuscript received 24 January 2024; revised 5 April 2024; accepted 8 April 2024. Date of publication 16 April 2024; date of current version 16 May 2024. This work was supported in part by the National Science and Technology Council of Taiwan under Grant 111-2221-E-005-034-MY2 and Grant 113-2622-8-005-004-TE1, in part by 2022 Kobe University Strategic International Collaborative Research Grants, and in part by Japan Science and Technology Agency. Recommended for publication by Associate Editor B. Shao. (Corresponding author: Ching-Ming Lai.)

Shiqiang Liu, Guiyi Dong, and Tomokazu Mishima are with the Division of Marine Technologies and Engineering, Faculty of Oceanology, Kobe University, Hyogo 6580022, Japan (e-mail: 218w903w@stu.kobe-u.ac.jp; 205w902w@stu.kobe-u.ac.jp; mishima@maritime.kobe-u.ac.jp).

Ching-Ming Lai is with the Department of Electrical Engineering, National Chung Hsing University, Taichung 402, Taiwan (e-mail: pecmlai@dragon.nchu.edu.tw).

Color versions of one or more figures in this article are available at <https://doi.org/10.1109/TPEL.2024.3389052>.

Digital Object Identifier 10.1109/TPEL.2024.3389052

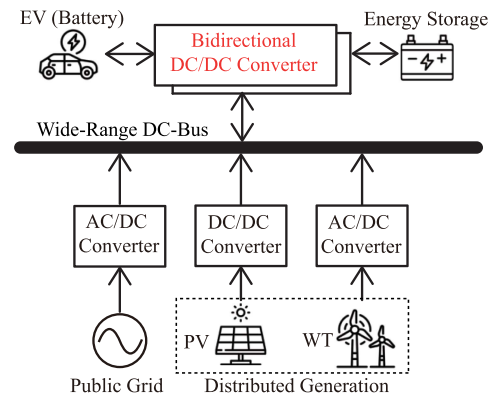


Fig. 1. System architecture of EV-connected DC-microgrid.

equipped with rechargeable batteries offering the capability of serving as mobile electricity storage units [2]. This feature positions EVs as potential auxiliary sources of electricity, addressing additional demand and forming the foundation for vehicle-to-grid (V2G) and vehicle-to-everything (V2X) technologies [3], [4], [5], [6], [7]. Researchers are now exploring into the possibility of utilizing EV-connected dc-microgrids (EV-DCMGs) as a backup power source [8], [9], [10].

The architecture of an EV-DCMGs system is illustrated in Fig. 1. The bidirectional dc–dc converter (BDC) emerges as a significant unit for interfacing dc energy sources, such as EV battery packs or energy storage units, with the dc-bus. The typical dc-bus voltage is 400 V or higher [11], while the battery voltage of EVs usually ranges from 400 to 800 V. On the other hand, energy storage systems' voltage often varies from tens of volts to tens of kilovolts. Therefore, BDCs with a wide voltage conversion ratio are essential for directly interfacing with the energy storage systems and EV batteries [12], [13], [14], [15]. In particular, a high voltage ratio is also crucial for efficient energy utilization and power conversion in EV-DCMGs systems. The BDCs are primarily categorized into isolated and nonisolated types. Isolated converters, such as flyback and full bridge, achieve substantial voltage ratio by modifying the turns ratio of high-frequency transformer (HF-X). However, the leakage inductance of HF-X can inherently cause high voltage spikes on power devices. To address this technical issue,

circuit topologies such as full bridge BDCs with a flyback snubber circuit or an active clamp circuit have been proposed [16], [17]. These methods facilitate recycling of energy from the leakage inductor, but request for additional auxiliary components. In addition, misalignment between input and output voltages and the transformer's turns ratio can significantly increase switching losses due to increase of reactive power [18].

Nonisolated converters encompass conventional buck/boost, coupled inductor, switched capacitor, and multilevel converters [19], [20]. Coupled inductor converters, capable of high voltage ratio through turns ratio adjustment, still face challenges with leakage inductance [21]. The multilevel converters, offering high voltage ratio and low voltage stress on power semiconductors, require more components and complex control strategies. Conventional buck-boost converters are efficient and cost-effective for low-voltage applications while suffer from limitations in a voltage conversion range and high voltage stress, making them unsuitable for energy storage applications [22]. Due to interleaved dc-dc converter topologies can reduce the inductor current ripple, enhance power rating, and improve overall efficiency, thus it is widely adopted in dc-dc applications [23]. For bidirectional power conversion, two-phase interleaved buck/boost converters have been extensively studied. However, these converters have limited voltage ratio and are suitable only for scenarios where the input and output voltages do not change significantly. Switched capacitor converter structures, known for their simplicity and scalability, transfer energy of capacitors via different charging and discharging paths to achieve high voltage ratio [24], [25], [26]. To reduce the input current ripple, interleaved switched capacitor converters have been proposed. The converter in [27] achieved high voltage ratio through dual-stage cascading while incurred high voltage stresses, which will increase the switching losses and reduce the conversion efficiency. In addition, it can only achieve the inductor currents balance when the duty cycles are equal to 0.5. In [28], an interleaved technique was used to smooth low voltage side current ripple. However, the low voltage side current ripple is sensitive to the number of interleaved phases and the duty cycle of active switches. In addition, its achievable voltage conversion ratio is narrower than that of the existing topologies. A bidirectional converter with zero current ripple cell and an auxiliary capacitor cell was proposed in [29]. While the reported converter exhibits low current ripple, its relatively high device voltage stresses and moderate voltage conversion ratio make it less suitable for high-voltage EV battery systems. In [30], the converter adopts a three-phase interleaved cascade structure with switched capacitor cells to achieve low voltage stresses across power switches. However, due to the cascaded configurations of three stages, power conversion efficiency is lower. Converters in [31], [32], [33], [34], and [35] utilized multiple coupled inductors and built-in transformers, respectively, for achieving high voltage conversion ratios and soft switching. Although high voltage ratio can be obtained by adjusting the turns ratio of magnetic components, but faced limitations by transfer capabilities. Furthermore, the maximum voltage stress of capacitors in the topology [32], [33], [35] is very high. The converter presented in [36] incorporated

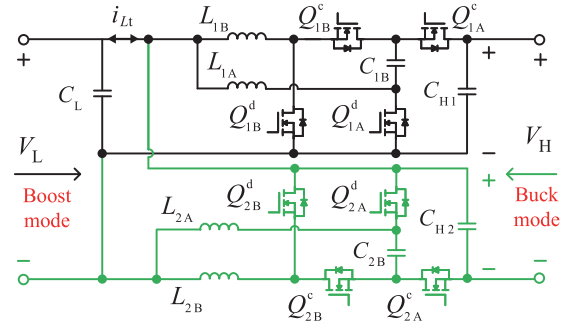


Fig. 2. Proposed F4P-ICPBDC topology.

a charge pump, offering enhanced characteristics in inductor current balance and reduced component count. Moreover, due to the adoption of Silicon-Carbide Metal-Oxide-Semiconductor Field-Effect Transistor (SiC-MOSFET), the converter efficiency can be expected over 97%. However, it is constrained by a narrow voltage conversion ratio, which is similar to the converter in [28], limiting its applicability in wide voltage ratio operations. In addition, it suffers from high maximum voltage stress, rendering it unsuitable for high-output-voltage applications.

In order to address these limitations of the existing BDCs, a new circuit topology and control scheme are introduced in this article; a switched capacitor-based floating four-phase interleaved charge-pump bidirectional dc-dc converter (F4P-ICPBDC) with asymmetrical duty limit control (A-DLC) strategy. The proposed interleaved BDC demonstrates a superior voltage ratio compared to those in [28], [29], and [30] and [36]. It also achieves naturally self-balancing of the inductor currents across the full duty cycle range both in buck and boost modes.

The rest of this article is organized as follows. Section II details the topology and control strategy of the proposed floating four-phase interleaved charge-pump bidirectional dc-dc converter. Section III is dedicated for analysis of the steady-state characteristics of the converter based on its operating principles. The parameters design guideline of the proposed BDCs are described in Section IV. Experimental results with a SiC-MOSFET-based 1 kW-50 kHz prototype are discussed in Section V, where the essential performances of the proposed BDC are demonstrated in details. Finally, Section VI concludes this article.

II. PROPOSED CONVERTER AND CONTROL STRATEGY WITH A-DLC

The proposed F4P-ICPBDC is presented in Fig. 2. It is composed of two sets of power semiconductor switches $Q_{1A}^c, Q_{1A}^d, Q_{1B}^c, Q_{1B}^d$ and $Q_{2A}^c, Q_{2A}^d, Q_{2B}^c, Q_{2B}^d$, charge-pump capacitors C_{1B} and C_{2B} , power inductors L_{1A}, L_{1B}, L_{2A} , and L_{2B} , low-voltage side filter capacitor C_L , and high-voltage side filter capacitors C_{H1} and C_{H2} . In order to simplify the analysis and design of the circuit parameters, the operating conditions of the main circuit are given as follows:

- 1) all the active and passive components are considered as ideal;

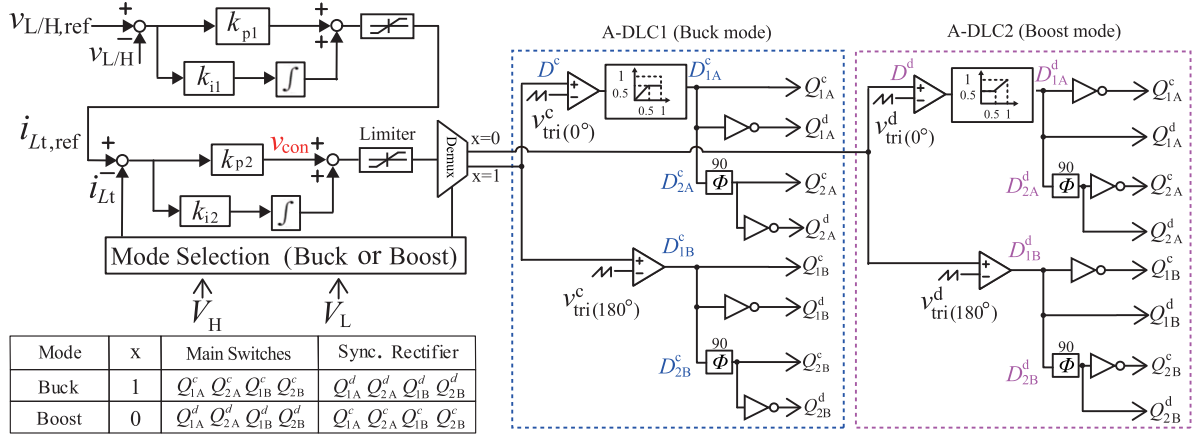


Fig. 3. Schematic diagram of controller based on A-DLC.

- 2) the dc inductor currents $i_{L_{1A}}, i_{L_{1B}}, i_{L_{2A}},$ and $i_{L_{2B}}$ are assumed to operate in continuous conduction mode (CCM);
- 3) the influence of load impedance is neglected in the steady-state analysis;
- 4) the voltages of capacitors are assumed to be well smoothed and constant, which implies that the voltage ripples can be neglected due to the sufficiently large capacitance.

Fig. 3 illustrates a closed-loop control strategy incorporating A-DLC. This controller is comprised of dual closed-loops of output voltage and total current of the interleaved inductors. Initially, the error between the sampled output voltage and the reference voltage undergoes external PI1 controller processing, which results in a reference current $i_{Lt,ref}$. Subsequently, the total current i_{Lt} of the four-phase inductors is detected and compared with the reference current. The internal PI2 controller is then employed to generate the control output v_{con} , with its range constrained between 0 and 1. Then, the preliminary duty cycle D^c or D^d of the active switches is determined through the demultiplexer on the basis of the input and output voltages as well as operation mode.

In the case of buck mode as an example, the control signal D^c is compared with a unit triangle carrier to derive duty cycle signals D_{1A}^c and D_{1B}^c . Subsequently, the signal D_{1A}^c undergoes the A-DLC1 to obtain the ultimate duty cycle for the active switches $Q_{1A}^c, Q_{1A}^d, Q_{2A}^c,$ and Q_{2A}^d . However, the signal D_{1B}^c directly yields the duty cycles of the active switches $Q_{1B}^c, Q_{1B}^d, Q_{2B}^c,$ and Q_{2B}^d . Moreover, the switches $Q_{1A}^c, Q_{2A}^c, Q_{1B}^c, Q_{2B}^c$ operate with a phase difference of 90° in sequence, while the counterpart $Q_{1A}^d, Q_{1B}^d, Q_{2A}^d,$ and Q_{2B}^d operate in the synchronous rectification (SR) state. A similar control logic is applicable to the boost mode. The pulse generation and control rules for the above switches are presented in Table I.

A. Buck Mode

The circuit configuration in the buck mode is shown in Fig. 4. The main switches $Q_{1A}^c, Q_{2A}^c, Q_{1B}^c, Q_{2B}^c$ are driven with the phase-shift angle of 90° in sequence, while the counterpart switches $Q_{1A}^d, Q_{2A}^d, Q_{1B}^d, Q_{2B}^d$ work as SR state to reduce the conduction power losses. Besides, the switch sets $Q_{1A}^c / Q_{1A}^d,$

TABLE I
RANGE OF DUTY CYCLES FOR BUCK AND BOOST MODES

Switches	Buck mode	Boost mode
Q_{1A}^c	$D_{1A}^c \leq 0.5$	$D_{1A}^c = 1 - D_{1A}^d$
Q_{1A}^d	$D_{1A}^d = 1 - D_{1A}^c$	$0.5 \leq D_{1A}^d$
Q_{1B}^c	$0 < D_{1B}^c < 1$	$D_{1B}^c = 1 - D_{1B}^d$
Q_{1B}^d	$D_{1B}^d = 1 - D_{1B}^c$	$0 < D_{1B}^d < 1$
Q_{2A}^c	$D_{2A}^c \leq 0.5$	$D_{2A}^c = 1 - D_{2A}^d$
Q_{2A}^d	$D_{2A}^d = 1 - D_{2A}^c$	$0.5 \leq D_{2A}^d$
Q_{2B}^c	$0 < D_{2B}^c < 1$	$D_{2B}^c = 1 - D_{2B}^d$
Q_{2B}^d	$D_{2B}^d = 1 - D_{2B}^c$	$0 < D_{2B}^d < 1$

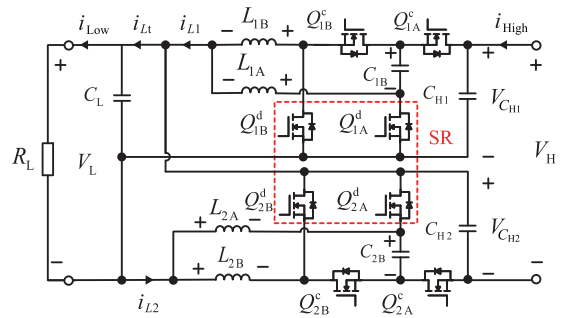


Fig. 4. Circuit configuration of F4P-ICPBDC in the buck mode.

$Q_{1B}^c / Q_{1B}^d, Q_{2A}^c / Q_{2A}^d,$ and Q_{2B}^c / Q_{2B}^d operate in complementary manner of gate driving, respectively. Furthermore, the charge pump capacitors C_{1B} and C_{2B} serve to step down the output voltage. The duty cycles of main switches are expressed as

$$\begin{cases} D_{1A}^c = D_{2A}^c = \begin{cases} D^c & \text{when } D^c < 0.5 \\ 0.5 & \text{when } D^c \geq 0.5 \end{cases} \\ D_{1B}^c = D_{2B}^c = D^c. \end{cases} \quad (1)$$

The typical operating waveforms of the main circuit for the buck mode are depicted in Fig. 5. Referring to these waveforms, the switching one cycle is divided into eight intervals as demonstrated in Fig. 6. The operating principle in the buck mode is described as follows when A-DLC1 is in active [Fig. 5(b)]:

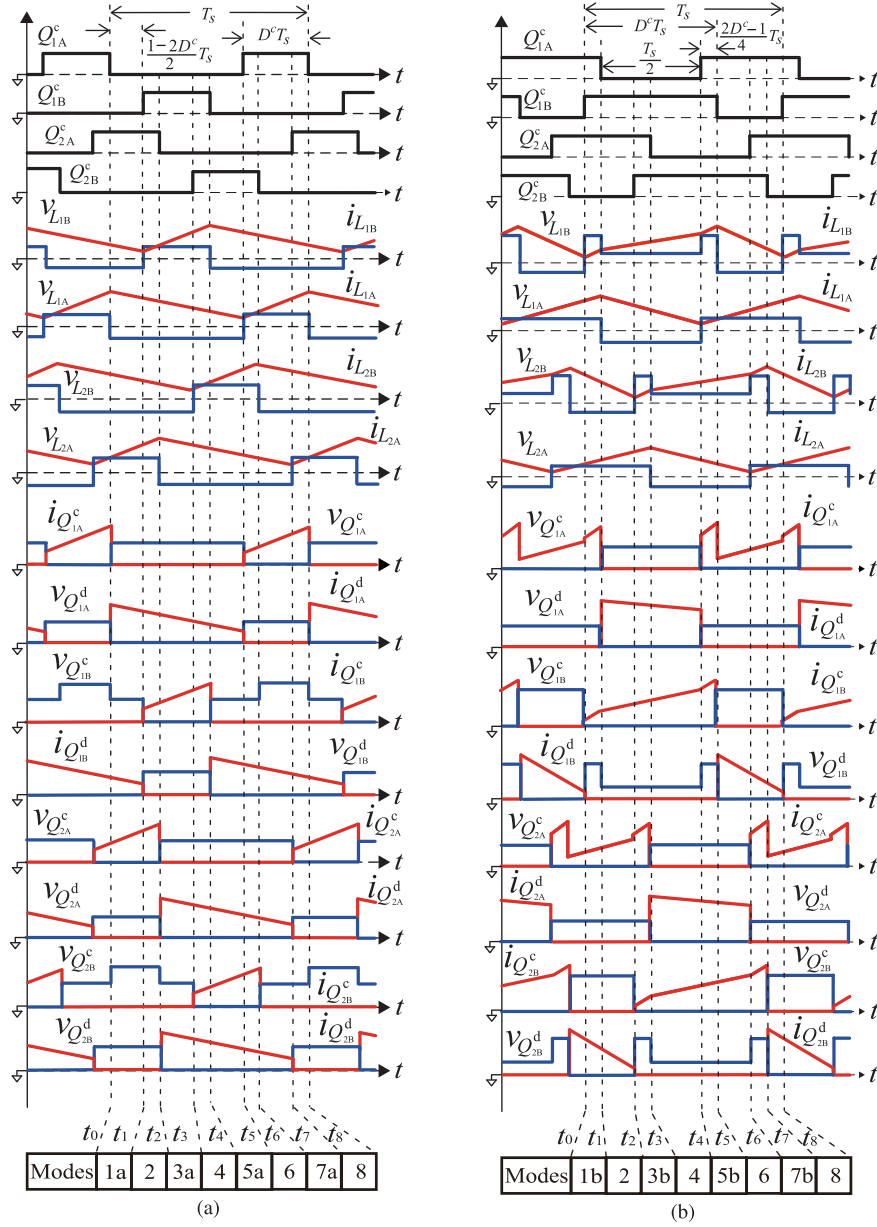


Fig. 5. Typical waveforms of F4P-ICPBDC in a buck mode, (a) $D^c < 0.5$ and (b) $D^c \geq 0.5$.

[Mode 1b] ($t_0 \leq t < t_1$): The active switch Q_{1B}^d which is operating in SR is turned OFF at $t = t_0$, and in a short interval the main switch Q_{1B}^c in the positive dc rail is turned ON. Thus, the dc inductor L_{1B} begins to store the magnetic energy and its current $i_{L_{1B}}$ linearly increases.

[Mode 2] ($t_1 \leq t < t_2$): The main switch Q_{1A}^c in the positive dc rail is turned OFF at $t = t_1$, and in a short time interval Q_{1A}^d is turned ON by SR. Accordingly, the dc inductor current $i_{L_{1A}}$ increases its positive gradient due to $V_{C_{1B}} > V_L$, while $i_{L_{2B}}$ keeps discharging.

[Mode 3b] ($t_2 \leq t < t_3$): The SR switch Q_{2B}^d is turned OFF at $t = t_2$, after which Q_{2B}^c in the negative dc rail is turned ON. Thus, the magnetic energy in the dc inductor L_{2B} is stored, thereby $i_{L_{2B}}$ begins to increase linearly.

[Mode 4] ($t_3 \leq t < t_4$): The main switch Q_{2A}^c in the negative dc rail is turned OFF at $t = t_3$, after which Q_{2A}^d is turned ON by SR. Then, the dc inductor current $i_{L_{2B}}$ keeps increasing linearly due to $V_{C_{2B}} > V_L$.

[Mode 5b] ($t_4 \leq t < t_5$): The SR switch Q_{1A}^d is turned OFF at $t = t_4$, and in a short interval the switch Q_{1A}^c in the positive dc rail is turned ON. Accordingly, the dc inductor current $i_{L_{1A}}$ changes to increase linearly.

[Mode 6] ($t_5 \leq t < t_6$): The main switch Q_{1B}^c in the positive dc rail is turned OFF at $t = t_5$, after which Q_{1B}^d is turned ON by SR. [Mode 7b] ($t_6 \leq t < t_7$): The SR switch Q_{2A}^d is turned OFF at $t = t_6$, after which the active switch Q_{2A}^c on the negative dc rail is turned ON. Then, the magnetic energy is stored at L_{2A} , whereby the dc inductor current $i_{L_{2A}}$ begins to linearly increase.

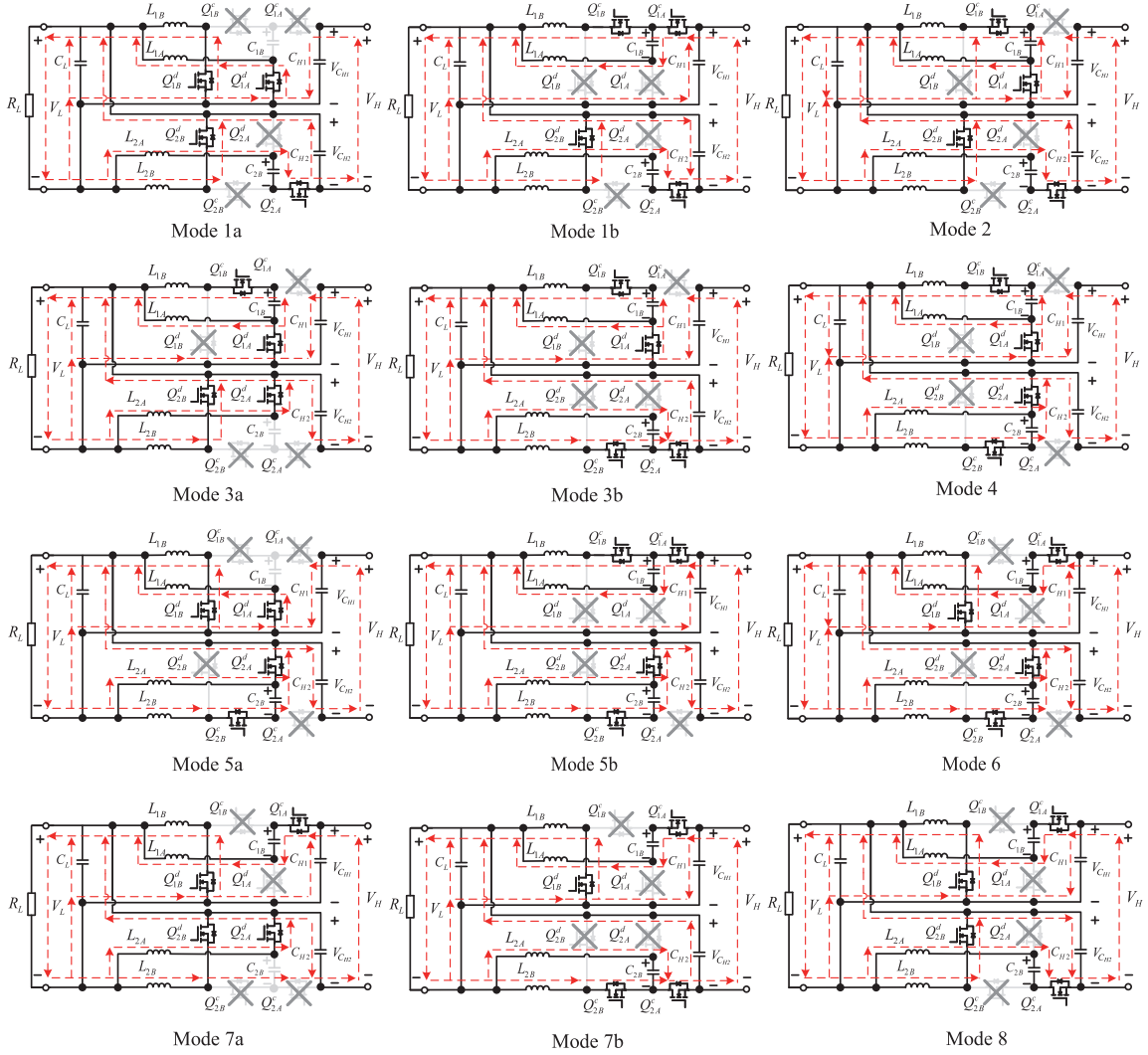


Fig. 6. Mode transitions and equivalent circuits during the switching one cycle in a buck mode.

[Mode 8] ($t_7 \leq t < t_8$): The active switch Q_{2B}^c on the negative dc rail is turned OFF at $t = t_7$, and in the short interval the counterpart Q_{2B}^d is turned ON by SR. Then, the dc inductor current $i_{L_{2B}}$ starts to decline linearly.

B. Boost Mode

The circuit configuration of F4P-ICPBDC in the boost mode is shown in Fig. 7. The main switches $Q_{1A}^d, Q_{2A}^d, Q_{1B}^d, Q_{2B}^d$ are driven with the phase-shift angle of 90° in sequence, meanwhile the active switches $Q_{1A}^c, Q_{2A}^c, Q_{1B}^c, Q_{2B}^c$ work as SR state to improve the conversion efficiency. The sets of switches $Q_{1A}^c / Q_{1A}^d, Q_{1B}^c / Q_{1B}^d, Q_{2A}^c / Q_{2A}^d$ and Q_{2B}^c / Q_{2B}^d operate in complementary manner, respectively. The charge pump capacitors C_{1B} and C_{2B} serve to step up the voltage from V_L to V_H . The duty cycles of main switches are expressed as

$$\begin{cases} D_{1A}^d = D_{2A}^d = \begin{cases} 0.5 & \text{when } D^d \leq 0.5 \\ D^d & \text{when } D^d > 0.5 \end{cases} \\ D_{1B}^d = D_{2B}^d = D^d. \end{cases} \quad (2)$$

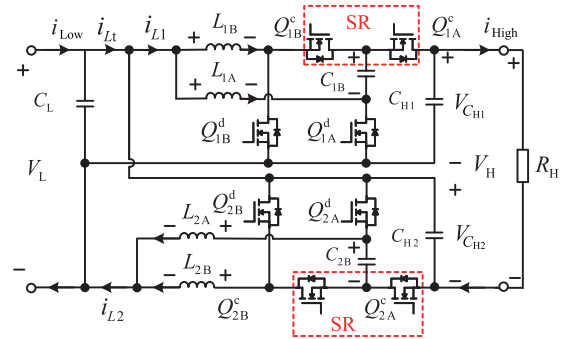


Fig. 7. Circuit configuration of F4P-ICPBDC in the boost mode.

The typical gate signals and voltage and current waveforms for the boost mode are depicted in Fig. 8. Referring to these waveforms, the switching one cycle is divided into eight intervals as demonstrated in Fig. 9. The operating principle in the boost mode is described as follows when A-DLC2 is active [Fig. 8(a)]: [Mode 1a] ($t_0 \leq t < t_1$): The main switch Q_{1B}^d is turned OFF at $t = t_0$, after which Q_{1B}^c in the positive dc rail is turned ON

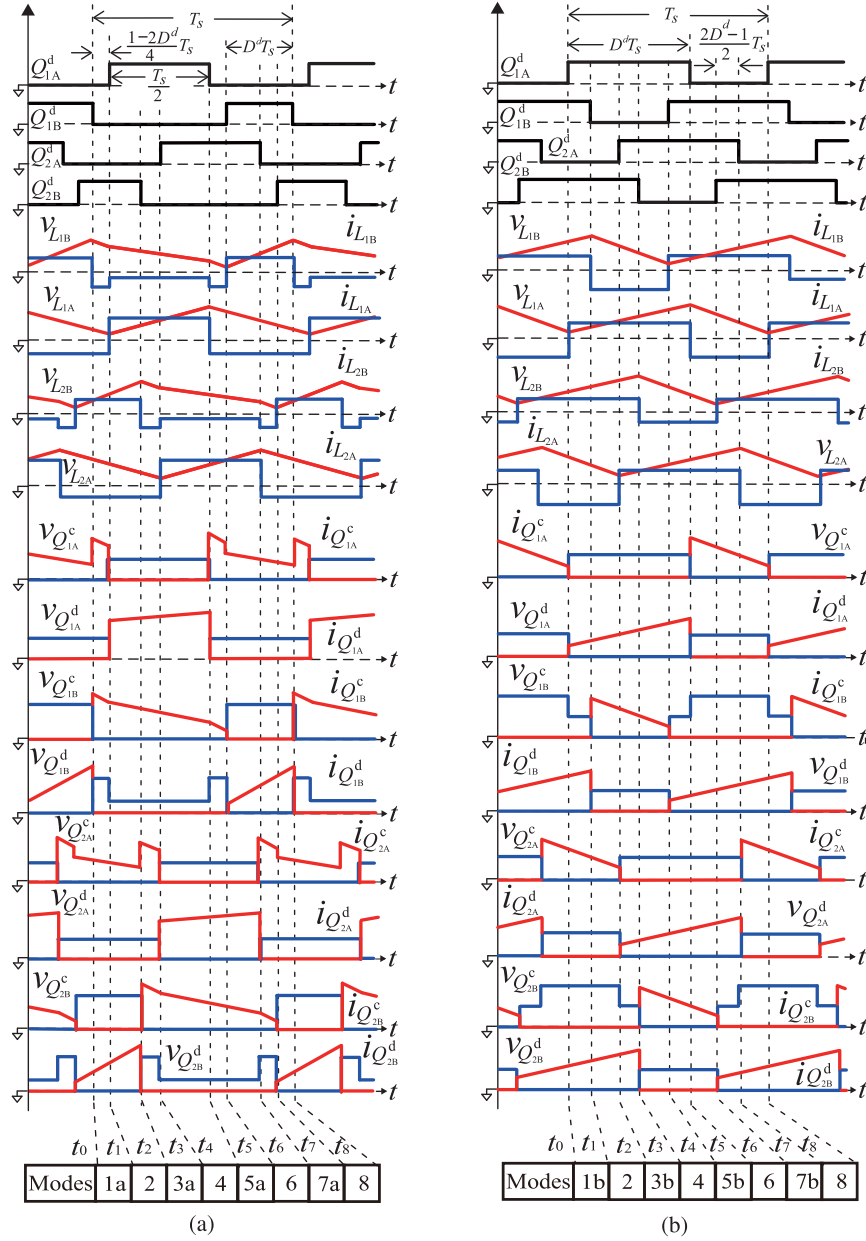


Fig. 8. Typical waveforms of F4P-ICPBDC in a boost mode. (a) $D^d \leq 0.5$ and (b) $D^d > 0.5$.

by SR. Then, the magnetic energy of L_{1B} begins to be released to the high voltage side V_H , whereby the current $i_{L_{1B}}$ decline linearly. The circuit operation is returned to Mode 2 at $t = t_1$.

[Mode 2] ($t_1 \leq t < t_2$): The SR switch Q_{1A}^c in the positive dc rail is turned OFF at $t = t_1$, after which the counterpart main switch Q_{1A}^d is turned ON. Then, dc inductor currents $i_{L_{1A}}$ increases gradually.

[Mode 3a] ($t_2 \leq t < t_3$): The main switch Q_{2B}^d is turned OFF at $t = t_2$, and Q_{2B}^c on the negative dc rail is turned ON by SR. Then, the magnetic energy in L_{2B} begins to be released to the high voltage side and $i_{L_{2B}}$ decline linearly.

[Mode 4] ($t_3 \leq t < t_4$): The SR switch Q_{2A}^c in the negative dc rail is turned OFF at $t = t_3$, and the main switch Q_{2A}^d is turned ON. The dc inductor L_{2A} begins to store magnetic energy via C_L , thereby $i_{L_{2A}}$ rises linearly.

[Mode 5a] ($t_4 \leq t < t_5$): The main switch Q_{1A}^d is turned OFF at $t = t_4$, after which Q_{1A}^c in the positive dc rail is turned ON by SR. Then, the magnetic energy in L_{1A} is released to the output side V_H by discharging of C_{1B} , and $i_{L_{1A}}$ begins to decline with a certain slope.

[Mode 6] ($t_5 \leq t < t_6$): The SR switch Q_{1B}^c in the positive dc rail is turned OFF at $t = t_5$, and in the short interval the main Q_{1B}^d is turned ON. Accordingly, the magnetic energy in L_{1B} begins to store, as a result $i_{L_{1B}}$ starts to increase linearly.

[Mode 7a] ($t_6 \leq t < t_7$): The main switch Q_{2A}^d is turned OFF at $t = t_6$, and Q_{2A}^c in the negative dc rail is turned ON by SR. Then, the magnetic energy in L_{2A} is released to the high voltage side, whereby $i_{L_{2A}}$ decreases with a certain slope.

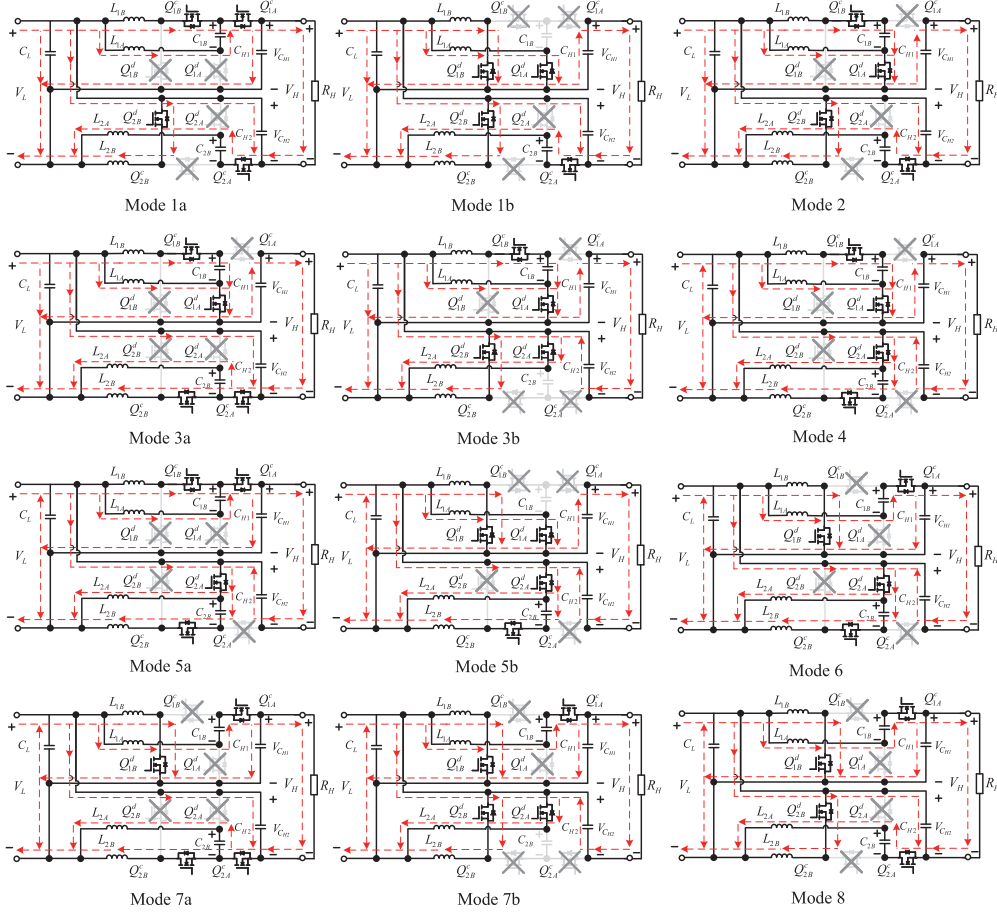


Fig. 9. Mode transitions and equivalent circuits during the switching one cycle in a boost mode.

[Mode 8] ($t_7 \leq t < t_8$): The SR switch Q_{2B}^c in the negative dc rail is turned OFF at $t = t_7$, followed by the turn ON of the main switch Q_{2B}^d . Accordingly, the dc inductor L_{2B} starts to store the magnetic energy, whereby the dc inductor current $i_{L_{2B}}$ begins to increase linearly.

$$I_{L_{1B}} = I_{L_{2B}} = \begin{cases} \frac{I_{Low} + I_{High}}{4} & \text{when } D^c < 0.5 \\ \frac{(1 - D_A^c)(I_{Low} + I_{High})}{2} & \text{when } D^c \geq 0.5 \end{cases} \quad (4)$$

III. STEADY-STATE ANALYSIS

A. Inductor Current Self-Balancing With A-DLC

1) *Buck Mode*: It is assumed here that the duty cycles of the main switches Q_{1A}^c and Q_{2A}^c are represented by D_A^c while those of Q_{1B}^c and Q_{2B}^c are represented by D_B^c , with both D_A^c and D_B^c equal to D^c . By applying the ampere-second balance principle on capacitors C_{1B} , C_{2B} , C_{H1} , C_{H2} , and C_L for the buck mode, the dc components of the current through L_{1A} , L_{1B} , L_{2A} , and L_{2B} can be expressed theoretically as

$$I_{L_{1A}} = I_{L_{2A}} = \begin{cases} \frac{I_{Low} + I_{High}}{4} & \text{when } D^c < 0.5 \\ \frac{D_A^c (I_{Low} + I_{High})}{2} & \text{when } D^c \geq 0.5 \end{cases}$$

where I_{Low} and I_{High} represent the low-voltage side load current, and the high-voltage side source current, respectively. It can be observed from (3) and (4) that condition in (1) should be satisfied in order to achieve balance of the inductor currents within the full range of duty cycle. At this point, the average inductor current can be represented as follows:

$$\begin{aligned} I_{L_{1A}} &= I_{L_{1B}} = I_{L_{2A}} = I_{L_{2B}} \\ &= I_{L_{A,B}} = \frac{I_{Low} + I_{High}}{4} = \frac{V_L}{R_L(4 - D^c)}. \end{aligned} \quad (5)$$

2) *Boost Mode*: It is assumed here that the duty cycles of main switches Q_{1A}^d and Q_{2A}^d are represented by D_A^d while those of Q_{1B}^d and Q_{2B}^d are expressed by D_B^d , where D_A^d and D_B^d are identical with D^d . In a similar manner, applying the ampere-second balance into C_{1B} , C_{2B} , C_{H1} , C_{H2} , and C_L for the boost mode yield the dc components of dc inductors L_{1A} ,

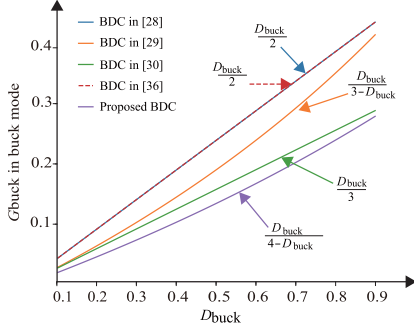


Fig. 10. Theoretical curves of DC voltage ratio in the buck mode.

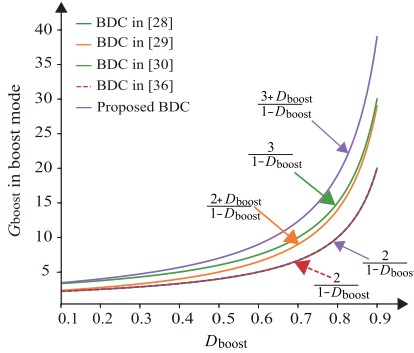


Fig. 11. Theoretical curves of DC voltage ratio in the boost mode.

 TABLE II
 VOLTAGE STRESSES OF ACTIVE SWITCHES IN BUCK MODE

Duty cycle		$0 < D^c < 0.5$	$0.5 \leq D^c < 1$
Voltage stresses	Q_{1A}^c, Q_{2A}^c	$\frac{V_H}{4 - D^c}$	$\frac{2D^c V_H}{4 - D^c}$
	Q_{1B}^c, Q_{2B}^c	$\frac{2V_H}{4 - D^c}$	$\frac{2V_H}{4 - D^c}$
	Q_{1A}^d, Q_{2A}^d	$\frac{V_H}{4 - D^c}$	$\frac{2D^c V_H}{4 - D^c}$
	Q_{1B}^d, Q_{2B}^d	$\frac{V_H}{4 - D^c}$	$\frac{2V_H}{4 - D^c}$

L_{1B}, L_{2A}, L_{2B} as expressed by

$$I_{L_{1A}} = I_{L_{2A}} = \begin{cases} \frac{(1-D_A^d)(I_{Low} + I_{High})}{2} & \text{when } D^d \leq 0.5 \\ \frac{I_{Low} + I_{High}}{4} & \text{when } D^d > 0.5 \end{cases} \quad (6)$$

$$I_{L_{1B}} = I_{L_{2B}} = \begin{cases} \frac{D_A^d(I_{Low} + I_{High})}{2} & \text{when } D^d \leq 0.5 \\ \frac{I_{Low} + I_{High}}{4} & \text{when } D^d > 0.5 \end{cases} \quad (7)$$

where I_{Low} and I_{High} represent the low-voltage side source current and the high-voltage side load current, respectively. In the similar way, it can be observed from (6) and (7) that condition in (2) should be satisfied so as to achieve balance of the inductor currents within the full range of duty cycle. At this point, the

 TABLE III
 VOLTAGE STRESSES OF ACTIVE SWITCHES IN BOOST MODE

Duty cycle		$0 < D^d \leq 0.5$	$0.5 < D^d < 1$
Voltage stresses	Q_{1A}^c, Q_{2A}^c	$2V_L$	$\frac{V_L}{1 - D^d}$
	Q_{1B}^c, Q_{2B}^c	$\frac{2V_L}{1 - D^d}$	$\frac{2V_L}{1 - D^d}$
	Q_{1A}^d, Q_{2A}^d	$2V_L$	$\frac{V_L}{1 - D^d}$
	Q_{1B}^d, Q_{2B}^d	$\frac{2V_L}{1 - D^d}$	$\frac{V_L}{1 - D^d}$

average inductor current can be represented as follows:

$$\begin{aligned} I_{L_{1A}} &= I_{L_{1B}} = I_{L_{2A}} = I_{L_{2B}} = I_{L_{A,B}} \\ &= \frac{I_{Low} + I_{High}}{4} = \frac{V_H}{R_H(1 - D^d)}. \end{aligned} \quad (8)$$

Therefore, it can be known from (5) and (8) that the dc inductor currents are naturally balanced with the aid of A-DLCs.

B. Voltage Conversion Ratio in Steady-State

1) *Buck Mode*: By applying the voltage-second balance principle into L_{1A}, L_{1B}, L_{2A} , and L_{2B} based on (44) and (45) introduced in the Appendix, the voltage conversion ratio can be derived as

$$G_{buck} = \frac{V_L}{V_H} = \begin{cases} \frac{D^c}{4 - D^c} & \text{when } D^c \leq 0.5 \\ \frac{D_A^c D_B^c}{2 - D_A^c D_B^c} = \frac{D^c}{4 - D^c} & \text{when } D^c > 0.5. \end{cases} \quad (9)$$

2) *Boost Mode*: Similarly, applying the voltage-second balance principle to L_{1A}, L_{1B}, L_{2A} , and L_{2B} based on (46) and (47) in the Appendix, the voltage conversion ratio can be expressed as

$$G_{boost} = \frac{V_H}{V_L} = \begin{cases} \frac{1 + D_A^d + D_B^d - D_A^d D_B^d}{(1 - D_A^d)(1 - D_B^d)} = \frac{3 + D^d}{1 - D^d} & \text{when } D^d < 0.5 \\ \frac{3 + D^d}{1 - D^d} & \text{when } D^d \geq 0.5. \end{cases} \quad (10)$$

According to (9) and (10), the voltage conversion ratios of the proposed and existing BDCs in the literatures [28], [29], [30], [36] are illustrated in Figs. 10 and 11. It is evident that the available voltage conversion ratios of the proposed BDC is much wider than those of other BDCs both in the buck and boost modes. The voltage conversion ratio G_{buck} attains in the range between 0.053 and 0.25 for $0.2 < D^c < 0.8$ in the buck mode. The voltage ratio G_{boost} covers the range from 4 to 19 for $0.2 < D^d < 0.8$ in the boost mode. Thus, it is revealed from Figs. 10 and 11 that the proposed BDC topology is advantageous over the others in terms of dc voltage ratio.

C. Analysis of Voltage Stresses on Power Devices

1) *Buck Mode*: Applying the ampere-second balance principle to C_{1B}, C_{2B}, C_{H1} , and C_{H2} based on (44) and (45) introduced

in the Appendix, the voltage across the capacitors can be determined as

$$V_{C_{1B}} = V_{C_{2B}} = \begin{cases} \frac{V_H}{4-D^c} & \text{when } D^c < 0.5 \\ \frac{2(1-D^c)V_H}{4-D^c} & \text{when } D^c \geq 0.5 \end{cases} \quad (11)$$

$$V_{C_{H1}} = V_{C_{H2}} = \frac{2V_H}{4-D^c} = \frac{V_H + V_L}{2}. \quad (12)$$

By employing (11) and (12) into the state equations for the buck mode, the voltage stresses of active switches can be derived as

$$\left\{ \begin{array}{l} \left\{ \begin{array}{l} V_{Q_{1A}^c} = V_{Q_{1A}^d} = V_{Q_{2A}^c} = V_{Q_{2A}^d} \\ = V_{Q_{1B}^d} = V_{Q_{2B}^d} = \frac{V_H}{4-D^c} \\ V_{Q_{1B}^c} = V_{Q_{2B}^c} = \frac{2V_H}{4-D^c} = \frac{V_H+V_L}{2} \end{array} \right. \text{when } D^c < 0.5 \\ \left\{ \begin{array}{l} V_{Q_{1A}^c} = V_{Q_{1A}^d} = V_{Q_{2A}^c} = V_{Q_{2A}^d} \\ = V_{Q_{1B}^d} = V_{Q_{2B}^d} = \frac{2D^c V_H}{4-D^c} \\ V_{Q_{1B}^c} = V_{Q_{2B}^c} = V_{Q_{1B}^d} \\ = V_{Q_{2B}^d} = \frac{2V_H}{4-D^c} = \frac{V_H+V_L}{2} \end{array} \right. \text{when } D^c \geq 0.5 \end{array} \right. \quad (13)$$

The maximum voltage stresses of the power devices are displayed for the buck mode in Table II.

2) *Boost Mode*: In the similar way, by applying the ampere-second balance principle to C_{1B} and C_{2B} , C_{H1} and C_{H2} based on (46) and (47) of the Appendix, the capacitors voltages can be determined as

$$V_{C_{1B}} = V_{C_{2B}} = \begin{cases} \frac{2D^d V_L}{1-D^d} & \text{when } D^d \leq 0.5 \\ \frac{V_L}{1-D^d} & \text{when } D^d > 0.5 \end{cases} \quad (14)$$

$$V_{C_{H1}} = V_{C_{H2}} = \frac{2V_L}{1-D^d} = \frac{V_H + V_L}{2}. \quad (15)$$

By substituting (14) and (15) for the state equations, the voltage stresses of active switches in the boost mode can be derived as

$$\left\{ \begin{array}{l} \left\{ \begin{array}{l} V_{Q_{1A}^c} = V_{Q_{1A}^d} = V_{Q_{2A}^c} \\ = V_{Q_{2A}^d} = 2V_L \\ V_{Q_{1B}^c} = V_{Q_{1B}^d} = V_{Q_{2B}^c} = V_{Q_{2B}^d} \\ = \frac{2V_L}{1-D^d} = \frac{V_H+V_L}{2} \end{array} \right. \text{when } D^d \leq 0.5 \\ \left\{ \begin{array}{l} V_{Q_{1A}^c} = V_{Q_{1A}^d} = V_{Q_{2A}^c} = V_{Q_{2A}^d} \\ = V_{Q_{1B}^d} = V_{Q_{2B}^d} = \frac{V_L}{1-D^d} \\ V_{Q_{1B}^c} = V_{Q_{2B}^c} \\ = \frac{2V_L}{1-D^d} = \frac{V_H+V_L}{2} \end{array} \right. \text{when } D^d > 0.5 \end{array} \right. \quad (16)$$

The maximum stress of the power devices is comprehensively presented for the boost mode in Table III.

D. Analysis of Inductor Current Ripples

1) *Buck Mode*: Taking the duty cycle range of $0 < D^c < 0.5$ into account, the current ripples of L_{1A} , L_{1B} , L_{2A} , and L_{2B} can

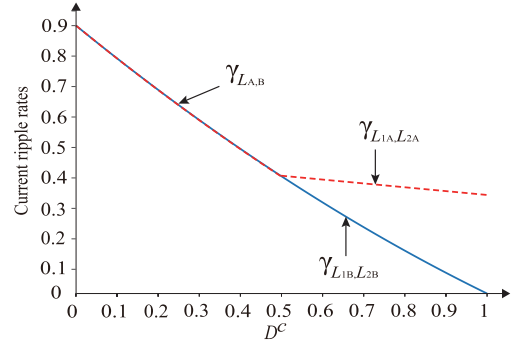


Fig. 12. Inductor current ripple rates versus duty cycle in the buck mode.

be derived in the buck mode as

$$\begin{aligned} \Delta i_{L_{1A}} &= \Delta i_{L_{2A}} = \Delta i_{L_{1B}} = \Delta i_{L_{2B}} \\ &= \Delta i_{L_{A,B}} = \frac{(1-D^c)V_L}{Lf_s}. \end{aligned} \quad (17)$$

By combining (5) and (17), the current ripple rate can be derived as follows:

$$\begin{aligned} \gamma_{L_{1A}, L_{2A}} &= \gamma_{L_{1B}, L_{2B}} = \gamma_{L_{A,B}} \\ &= \frac{\Delta i_{L_{A,B}}}{2I_{L_{A,B}}} = \frac{(1-D^c)(4-D^c)R_L}{2Lf_s}. \end{aligned} \quad (18)$$

In the similar way, the current ripples of L_{1A} , L_{1B} , L_{2A} and L_{2B} within the range of $0.5 \leq D^c < 1$ can be described as follows:

$$\Delta i_{L_{1A}} = \Delta i_{L_{2A}} = \Delta i_{L_A} = \frac{V_L}{2Lf_s} \quad (19)$$

$$\Delta i_{L_{1B}} = \Delta i_{L_{2B}} = \Delta i_{L_B} = \frac{(1-D^c)V_L}{Lf_s}. \quad (20)$$

Employing (5) to (19) and (20), respectively, the current ripple rates can be expressed as

$$\gamma_{L_{1A}, L_{2A}} = \frac{\Delta i_{L_A}}{2I_{L_{A,B}}} = \frac{(4-D^c)R_L}{4Lf_s} \quad (21)$$

$$\gamma_{L_{1B}, L_{2B}} = \frac{\Delta i_{L_B}}{2I_{L_{A,B}}} = \frac{(1-D^c)(4-D^c)R_L}{2Lf_s}. \quad (22)$$

The characteristics of current ripple rates in L_{1A} , L_{1B} , L_{2A} , and L_{2B} versus D^c are portrayed in Fig. 12 with a set of numerical values: $L_{1A} = L_{1B} = L_{2A} = L_{2B} = 219 \mu\text{H}$, the switching frequency $f_s = 50 \text{ kHz}$, $V_H = 400 \text{ V}$, and $V_L = 72 \text{ V}$. Since the rated power is set as 1 kW , the nominal load resistance is given as $R_L = 5.184 \Omega$. As the duty cycle increases, the ripple rates of the inductor current tends to decline. Within the range of $0.5 < D^c < 1$, the current ripples in the inductors L_{1B} and L_{2B} are smaller than those of L_{1A} and L_{2A} due to the effect of topology: (C_{1B} and C_{2B}).

2) *Boost Mode*: The current ripples of L_{1A} , L_{1B} , L_{2A} , and L_{2B} within the range of $0 < D^d \leq 0.5$ can be defined as

$$\Delta i_{L_{1A}} = \Delta i_{L_{2A}} = \Delta i_{L_A} = \frac{V_L}{2Lf_s} \quad (23)$$

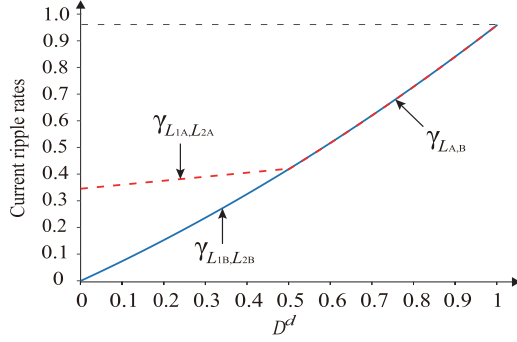


Fig. 13. Inductor current ripple rates versus duty cycle in the boost mode.

$$\Delta i_{L_{1B}} = \Delta i_{L_{2B}} = \Delta i_{L_B} = \frac{D^d V_L}{L f_s}. \quad (24)$$

Substituting (8) for (23) and (24), respectively, the current ripple rates can be derived as follows:

$$\gamma_{L_{1A},L_{2A}} = \frac{\Delta i_{L_A}}{2I_{L_{A,B}}} = \frac{(1-D^d)^2 R_H}{4(3+D^d)L f_s} \quad (25)$$

$$\gamma_{L_{1B},L_{2B}} = \frac{\Delta i_{L_B}}{2I_{L_{A,B}}} = \frac{D^d(1-D^d)^2 R_H}{2(3+D^d)L f_s}. \quad (26)$$

The current ripples of L_{1A} , L_{1B} , L_{2A} , and L_{2B} in the range of $0.5 < D^d < 1$ can also be described as

$$\Delta i_{L_{1A}} = \Delta i_{L_{2A}} = \Delta i_{L_{1B}} = \Delta i_{L_{2B}} = \Delta i_{L_{A,B}} = \frac{D^d V_L}{L f_s}. \quad (27)$$

Accordingly, combination (8) and (27) yields the current ripple rate as

$$\begin{aligned} \gamma_{L_{1A},L_{2A}} &= \gamma_{L_{1B},L_{2B}} = \gamma_{L_{A,B}} \\ &= \frac{\Delta i_{L_{A,B}}}{2I_{L_{A,B}}} = \frac{D^d(1-D^d)^2 R_H}{2(3+D^d)L f_s}. \end{aligned} \quad (28)$$

The characteristics of current ripple rates in L_{1A} , L_{1B} , L_{2A} , and L_{2B} versus D^d are shown in Fig. 13 with the same parameters as the buck mode mentioned above, except for the load resistance. In the boost mode, where the output power is likewise fixed at 1 kW, the load varies with the output voltage as expressed by

$$R_H = \frac{V_H^2}{P_o} = \frac{5.184(3+D^d)^2}{(1-D^d)^2}. \quad (29)$$

As the duty cycle increases, the ripple rates of the inductor currents exhibit increment trend. In the similar way, the current ripple rates in L_{1B} and L_{2B} within the range of $0 < D^d < 0.5$ are smaller than those of L_{1A} and L_{2A} , due to the effect of topology. It is worth noting that the inductor current ripple rate is not only related to the duty cycle, but also to the inductance value, operating frequency, and load resistance.

E. Robustness of Average Inductor Current

Fig. 14 showcases the simulation results illustrating the tolerance of the four-phase inductor variations for the average

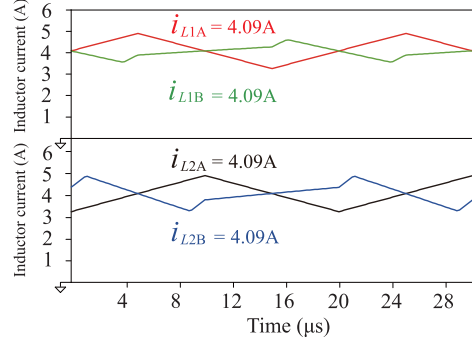


Fig. 14. Tolerances on the average inductor current for the DC inductor variations (400 V to 72 V, 1 kW).

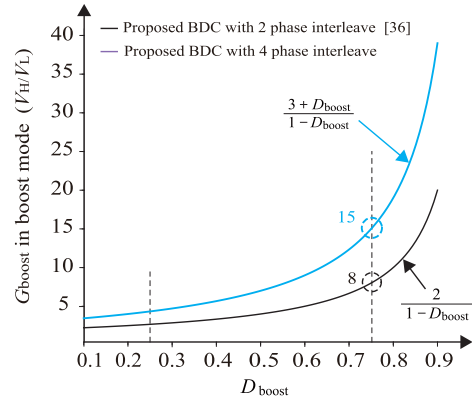


Fig. 15. Voltage conversion ratios versus duty cycle in the boost mode.

inductor current. As an example, the inductances of L_{1A} , L_{1B} , L_{2A} , and L_{2B} are set to $263 \mu\text{H}$ (1.2 times the nominal value), $219 \mu\text{H}$, $175 \mu\text{H}$ (0.8 times the nominal value) and $219 \mu\text{H}$ (the nominal value), respectively. The simulation results prove that the implementation of the A-DLC ensures the balance of the average inductor current in CCM, despite up to a 20% fluctuation in the inductance values. Consequently, the proposed BDC topology demonstrates remarkable robustness to variations of the dc inductors.

IV. DESIGN CONSIDERATION IN MAIN CIRCUIT

A. Selection of Interleaving Phase Numbers

Fig. 15 illustrates the relationship between voltage conversion ratio and duty cycle for both the two- and four-phase interleaved topologies in the boost mode. It can be observed that employing the four-phase interleaved topology can significantly enhance the voltage conversion ratio. Typically, the duty cycle of a buck/boost converter exists between 0.2 and 0.8 while occasionally between 0.3 and 0.7. Considering the ripple rates of the inductor currents in the boost mode as depicted in Fig. 13, it is reasonable to operate the converter's duty cycle between 0.25 and 0.75 to ensure that the inductor current operates in CCM and to maintain sufficient margin. When the duty cycle is at 0.75, the voltage ratio for the two-phase interleaved topology is 8, while it is 15 for the four-phase interleaved topology. Aiming to attain the voltage conversion from 72 V to 400 V–800 V, a voltage ratio

higher than 11.1 should be accomplished. In addition, further increasing the voltage ratio is necessary to maintain a 800 V output in consideration of presence of the loads. Moreover, when the input voltage in application scenarios is lower than 72 V such as 30 V as depicted in [30] and [33], a higher voltage ratio is required to achieve an output of 800 V. It is obvious from the viewpoints of voltage ratio that a four-phase interleaved topology is more suitable for the wide range of voltage ratio.

B. Selection of Active Switches

According to (13) and (16), the maximum voltage stress on the active switches is half the sum of the low-side and high-side voltages, in both buck and boost modes. Furthermore, it can be observed from the waveforms in Figs. 5 and 8 that the maximum current flowing through the active switches is two times the average inductor current. Therefore, the active switch should meet the following requirements as denoted by

$$\begin{cases} v_{ds} > \frac{V_H + V_L}{2} \\ i_{ds} > \begin{cases} \left(2 + \frac{4D^c - 2}{D^c} \gamma_{L_{1A}, L_{2A}}\right) I_{L_{A,B}} & \text{when } D^d \leq 0.5 \\ (1 + \gamma_{L_{A,B}}) I_{L_{A,B}} & \text{when } D^d > 0.5. \end{cases} \end{cases} \quad (30)$$

Considering to the scenario of 800 V in the high-voltage side, which is shared by two active switches, MOSFETs rated at 650 V and above are considered suitable for the active switches in the proposed BDC. In particular, the 650 V is the optimal choice from the viewpoints of low ON-resistance and low gate charging capacitance.

C. Determination of Operating Frequency

The maximum operating frequency of SiC-MOSFETs can reach up to several hundred kHz in the latest trend of the wide band-gap power devices, and increasing the operating frequency under the same power leads to substantial reduction of the volume of magnetic components. The main switches are commutated in a hard-switching state (e.g., Q_{1A}^c , Q_{2A}^c , Q_{1B}^c , and Q_{2B}^c in buck mode) at the current stage of this research, while the remaining switches operate soft commutations and behave SR. Hence, the switching frequency over a hundred kHz may induce significant amounts of switching losses in the main switches. Therefore, the operating frequency is selected as 50 kHz for the proposed BDC from the practical point of view.

D. Design of Inductors

The inductance values of L_{1A} , L_{1B} , L_{2A} , and L_{2B} can be obtained using the following equations:

$$\begin{cases} L_{1A} = L_{2A} = \frac{V_L D^d}{2\gamma_{L_{1A}, L_{2A}} I_{L_{A,B}} f_s} \\ L_{1B} = L_{2B} = \frac{V_L D^d}{2\gamma_{L_{1B}, L_{2B}} I_{L_{A,B}} f_s}. \end{cases} \quad (31)$$

In order to ensure that the inductor currents operate in CCM, the values of $\gamma_{L_{1A}, L_{2A}}$ and $\gamma_{L_{1B}, L_{2B}}$ must be less than 1. In

addition, the selected inductors should be able to accommodate the maximum current according to the following requirements:

$$\begin{cases} i_{L_{1A}} = i_{L_{2A}} > (1 + \gamma_{L_{1A}, L_{2A}}) I_{L_{A,B}} \\ i_{L_{1B}} = i_{L_{2B}} > (1 + \gamma_{L_{1B}, L_{2B}}) I_{L_{A,B}}. \end{cases} \quad (32)$$

E. Design of Capacitors

Assuming L_{1A} , L_{2A} , L_{1B} , and L_{2B} have the same values, the ripple current on the low voltage side in the four-phase interleaved topology can be approximately expressed as

$$\Delta I_{Low} = \begin{cases} \frac{(0.5 - D^d)V_H}{(3 + D^d)Lf_s} & 0 < D^d \leq 0.5 \\ \frac{(D^d - 0.5)(3 - 4D^d)V_H}{(3 + D^d)Lf_s} & 0.5 < D^d \leq 0.75 \\ \frac{(1 - D^d)(4D^d - 3)V_H}{(3 + D^d)Lf_s} & 0.75 < D^d < 1. \end{cases} \quad (33)$$

The maximum charge increment stored in C_L during one cycle in the buck mode is as

$$\Delta Q = \frac{\Delta I_{Low}}{8f_s}. \quad (34)$$

Therefore, the minimum capacitance value of C_L can be determined as

$$C_L = \frac{\Delta I_{Low}}{8\Delta V_{C_L} f_s}. \quad (35)$$

The charge-pump capacitors C_{1B} and C_{2B} can also be calculated as

$$C_{1B} \geq \text{MIN} \left(\frac{I_{L_{1B}}}{2\Delta V_{C_{1B}} f_s}, \frac{(1 - D^d)I_{L_{1B}}}{\Delta V_{C_{1B}} f_s} \right) \quad (36)$$

$$C_{2B} \geq \text{MIN} \left(\frac{I_{L_{2B}}}{2\Delta V_{C_{2B}} f_s}, \frac{(1 - D^d)I_{L_{2B}}}{\Delta V_{C_{2B}} f_s} \right). \quad (37)$$

Similarly, the filter capacitors of high-voltage side C_{H1} and C_{H2} can also be expressed as

$$C_{H1} \geq \text{MAX} \left(\frac{I_H}{2\Delta V_{C_{H1}} f_s}, \frac{D^d I_H}{\Delta V_{C_{H1}} f_s} \right) \quad (38)$$

$$C_{H2} \geq \text{MAX} \left(\frac{I_H}{2\Delta V_{C_{H2}} f_s}, \frac{D^d I_H}{\Delta V_{C_{H2}} f_s} \right). \quad (39)$$

F. ZVS Range

Referring to Figs. 5 and 6, it is evident that the minimum current through Q_{1A}^d and Q_{2A}^d equals that through Q_{1B}^d and Q_{2B}^d for $0 < D^c < 0.5$, while the minimum current flowing through Q_{1A}^d and Q_{2A}^d exceeds that through Q_{1B}^d and Q_{2B}^d for $0.5 \leq D^c < 1$. Consequently, when Q_{1B}^d and Q_{2B}^d meet the ZVS conditions, Q_{1A}^d and Q_{2A}^d naturally satisfy the ZVS conditions too. In order to ensure the successful completion of ZVS turn-ON and turn-OFF commutations in the buck mode with the SR switches, the minimum energy stored in the dc inductors L_{1B} and L_{2B} should completely discharge C_{oss} in Q_{1B}^d , Q_{2B}^d and

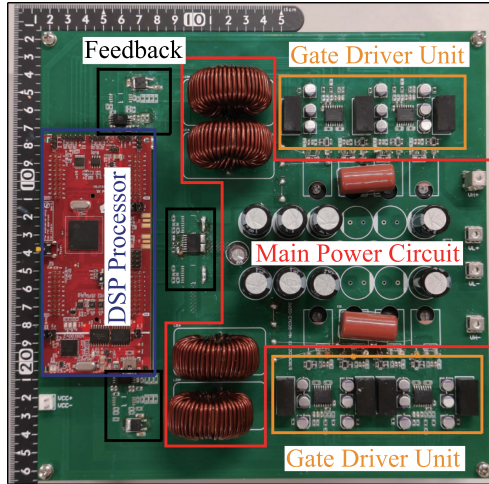


Fig. 16. Exterior appearance of 1 kW-50 kHz prototype.

charge in Q_{1B}^c , Q_{2B}^c as described by

$$\begin{cases} L_{1B} (i_{L_{1B}})^2 > C_{oss} (V_{Q_{1B,ds}^d})^2 + C_{oss} (V_{Q_{1B,ds}^c})^2 \\ L_{2B} (i_{L_{2B}})^2 > C_{oss} (V_{Q_{2B,ds}^d})^2 + C_{oss} (V_{Q_{2B,ds}^c})^2 \end{cases} \quad (40)$$

where C_{oss} represents the output capacitance of the power MOSFETs. Furthermore, by combining (5), (22) and (40), the critical load condition in the low-voltage side can be determined as

$$\left(\frac{(1-D^c)(4-D^c)}{2Lf_s} + \frac{4(4-D^c)}{D^c} \sqrt{\frac{C_{oss}}{2L}} \right) R_L = 1. \quad (41)$$

Referring to Figs. 8 and 9, the minimum current through Q_{1A}^c and Q_{2A}^c exceeds that through Q_{1B}^c and Q_{2B}^c for $0 < D^d \leq 0.5$, while they are identical for $0.5 < D^d < 1$. Therefore, once Q_{1B}^c and Q_{2B}^c meet the ZVS condition, Q_{1A}^c and Q_{2A}^c naturally satisfy the ZVS conditions. In order to ensure the successful completion of ZVS in the boost mode, it is also necessary to satisfy the essential condition that the minimum energy stored in inductor L_{1B} and L_{2B} fully discharges C_{oss} in Q_{1B}^c , Q_{2B}^c and charge in Q_{1B}^d , Q_{2B}^d as described by

$$\begin{cases} L_{1B} (i_{L_{1B}})^2 > C_{oss} (V_{Q_{1B,ds}^c})^2 + C_{oss} (V_{Q_{1B,ds}^d})^2 \\ L_{2B} (i_{L_{2B}})^2 > C_{oss} (V_{Q_{2B,ds}^c})^2 + C_{oss} (V_{Q_{2B,ds}^d})^2 \end{cases}. \quad (42)$$

Furthermore, by combining (8), (26), and (42), the critical load condition in the high-voltage side can be expressed as

$$\left(\frac{D^d(1-D^d)^2}{2(3+D^d)Lf_s} + \frac{4(1-D^d)}{3+D^d} \sqrt{\frac{C_{oss}}{2L}} \right) R_H = 1. \quad (43)$$

V. EXPERIMENTAL VERIFICATION

A performance of the F4P-ICPBDC is investigated by experiment of 1 kW-50 kHz prototype. The exterior appearance of the prototype is portrayed in Fig. 16, and the specifications are listed in Table IV, respectively. All the active switches

TABLE IV
SPECIFICATIONS OF THE F4P-ICPBDC CONVERTER

Item	Symbol	Value [unit]
High-side voltage	V_H	400 – 800 [V]
Low-side voltage	V_L	72 [V]
Output power rating	P_o	1 [kW]
Switching frequency	f_s	50 [kHz]
DC inductors	$L_{1A}, L_{1B},$ (HHBC24N-2R0A0219V) L_{2A}, L_{2B}	219 [μ H]/15A (Fe-Si)
High-side capacitors	C_{H1}, C_{H2}	272 [μ F]/500V
Low-side capacitor	C_L	600 [μ F]/100V
Charge pump capacitors	C_{1B}, C_{2B}	10 [μ F] /450V
Power MOSFETs	$Q_{1A}^c - Q_{2B}^d$	IMW65R027M1H
DSP controller chip		TMS320F28379D
Voltage sampling chip		AMC1311BDWR
Current sampling chip		CZ3A02

are implemented with SiC-MOSFETs (IMW65R027M1H, 650 V, 47 A, 27 m Ω , 244 pF), all of which are driven by isolated gate drivers (UCC21520, Texas Instruments). The power controller is comprised by a DSP board development kit (LAUNCHXL-F28379D, Texas Instruments) with TMS320F28379D micro-controller.

A. Steady-State Performances in the Buck Mode

1) 400 V to 72 V: Fig. 17 provides a detailed depiction of key experimental waveforms in a buck mode, where the dc input voltage V_H and the load resistance R_L are set as 400 V and 5.184 Ω , respectively. It can be observed in Fig. 17(a) that the sequential operation of the main switches Q_{1A}^c , Q_{2A}^c , Q_{1B}^c , and Q_{2B}^c attain with a phase shift angle of 90°. The duty cycles for Q_{1A}^c , Q_{2A}^c are consistently fixed at 0.5, while those for Q_{1B}^c and Q_{2B}^c are set at 0.63. The current waveforms of the dc inductors are shown in Fig. 17(b). The average currents for L_{1A} , L_{1B} , L_{2A} , and L_{2B} , are measured as $I_{L_{1A}} = 3.98$ A, $I_{L_{1B}} = 4.01$ A, $I_{L_{2A}} = 4.02$ A, and $I_{L_{2B}} = 3.97$ A respectively, thus a well-balanced average inductor current can be realized in the proposed BDC with A-DLC1. Moreover, the current ripples for $i_{L_{1A}}$, $i_{L_{1B}}$, $i_{L_{2A}}$, and $i_{L_{2B}}$ are observed as $\Delta I_{L_{1A}} = 3.19$ A, $\Delta I_{L_{1B}} = 2.49$ A, $\Delta I_{L_{2A}} = 3.26$ A, and $\Delta I_{L_{2B}} = 2.47$ A, respectively, which have good agreement with (19) and (20). The current ripple rates for these inductors are found to be 0.40, 0.31, 0.41, and 0.31, respectively, corresponding to the theoretical values in (21) and (22). These experimental results clarify the validity of the current ripple analysis for duty cycles in the range of $0.5 \leq D^c < 1$.

Fig. 17(c) shows that the current ripple rates for i_{L1} , and i_{L2} are further reduced to 0.16 and 0.15, respectively, due to the interleaved switching patterns. Moreover, the total current of the interleaved inductors, i_{Lt} has small current ripple rate, allowing for a reduction in the use of filtering capacitors. Fig. 17(d) presents the steady-state voltages across the capacitors. The measured values are, $V_{C_{1B}} = 94.5$ V, $V_{C_{2B}} = 94.5$ V, $V_{C_{H1}} = 236.2$ V, $V_{C_{H2}} = 233.7$ V, and $V_H = 400$ V, corresponding well with (11) and (12). In addition, the output voltage is controlled as $V_L = 72$ V in accordance with the command value, whereby the validity of (9) is revealed.

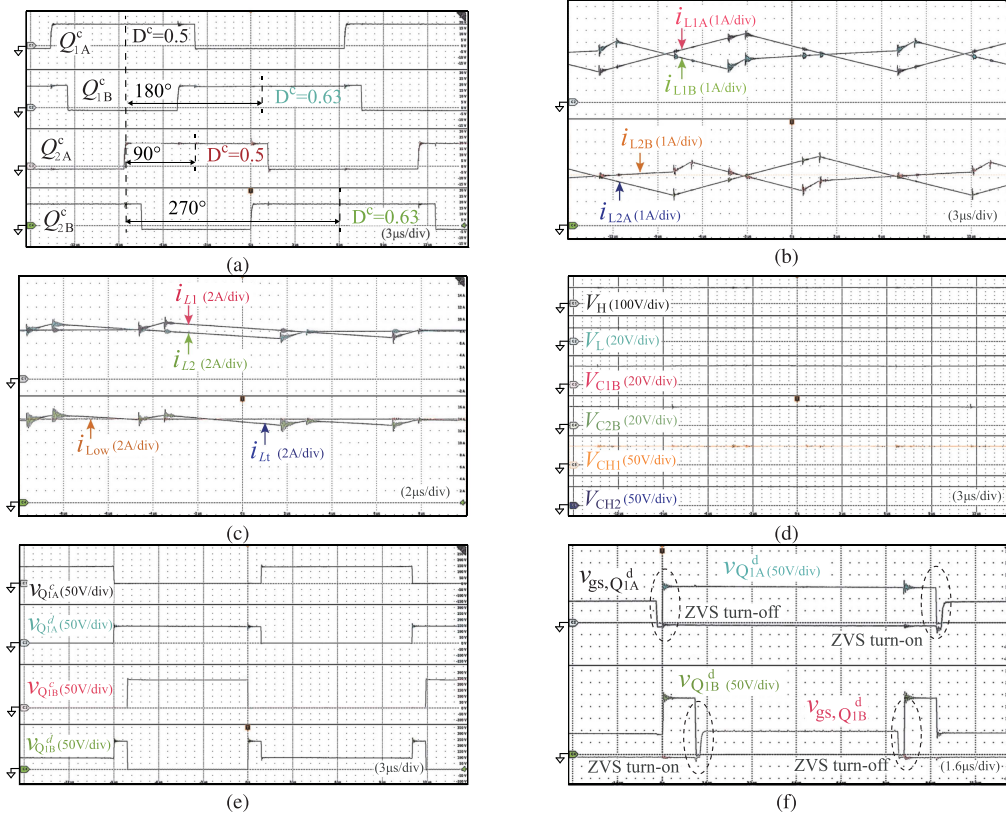


Fig. 17. Observed waveforms in a buck mode with $V_H = 400$ V and $R_L = 5.184 \Omega$ for $V_L = 72$ V: (a) gate signals, (b) DC inductor currents, (c) high and low-side unit DC inductor currents and the output currents, (d) capacitor voltages, (e) power switch voltage stresses, and (f) synchronous rectifier voltages.

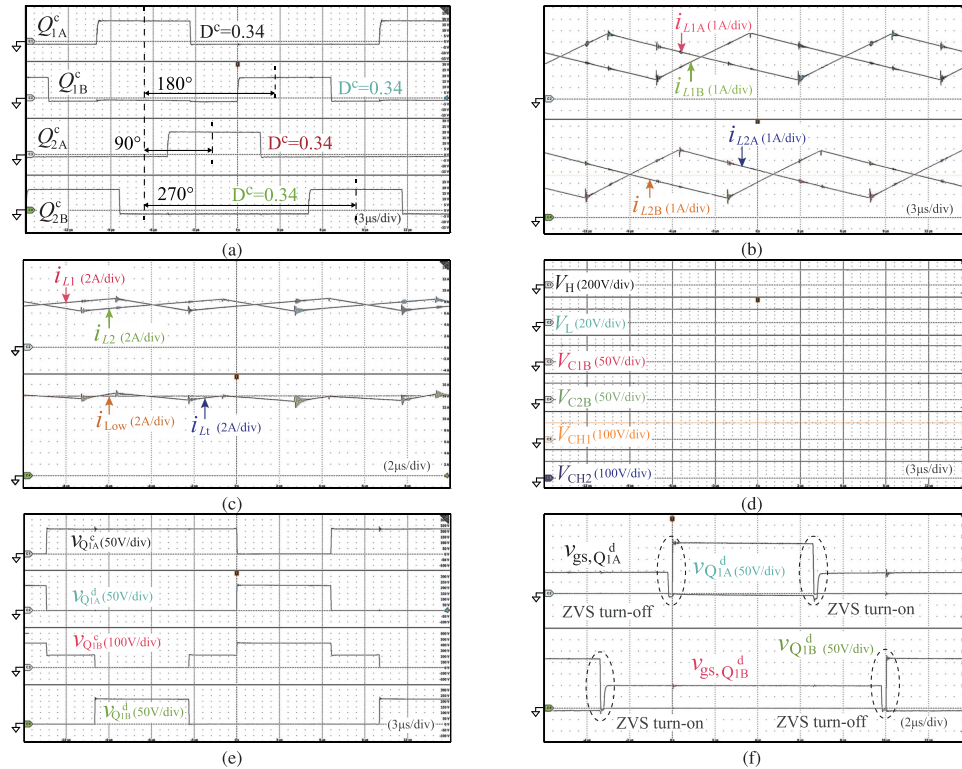


Fig. 18. Observed waveforms in a buck mode with $V_H = 800$ V and $R_L = 5.184 \Omega$ for $V_L = 72$ V: (a) gate signals, (b) DC inductor currents, (c) high and low-side unit DC inductor currents and the output currents, (d) capacitor voltages, (e) power switch voltage stresses, and (f) synchronous rectifier voltages.

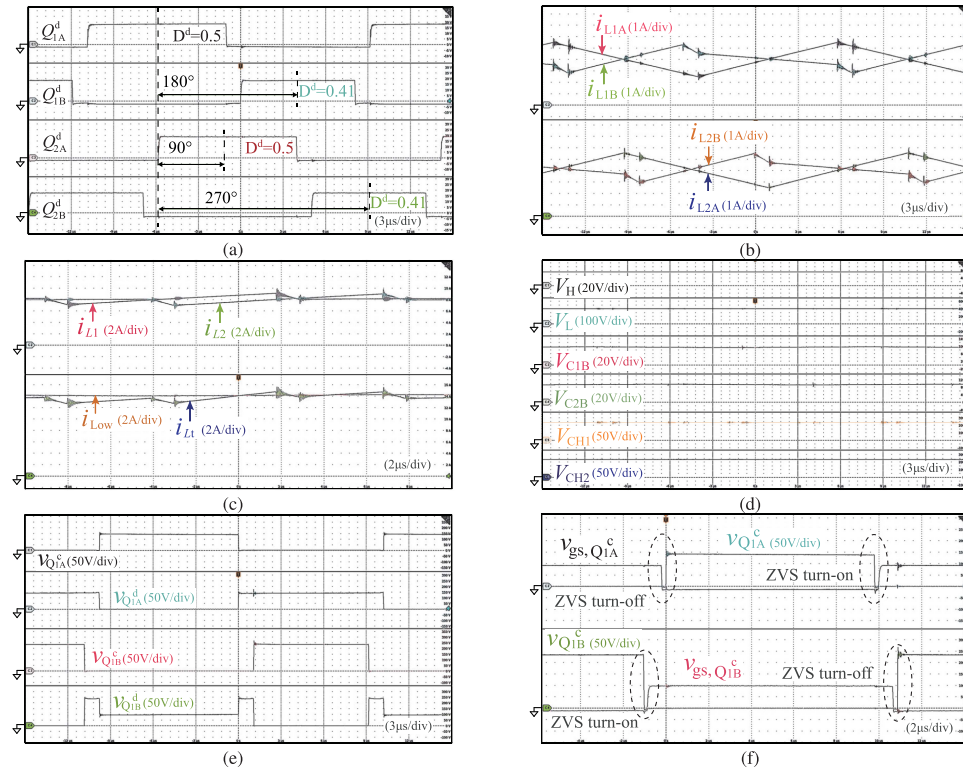


Fig. 19. Observed waveforms in a boost mode with $V_L = 72$ V and $R_H = 160$ Ω for $V_H = 400$ V: (a) gate signals, (b) DC inductor currents, (c) high and low-side unit DC inductor currents and the input currents, (d) capacitor voltages, (e) power switch voltage stresses, and (f) synchronous rectifier voltages.

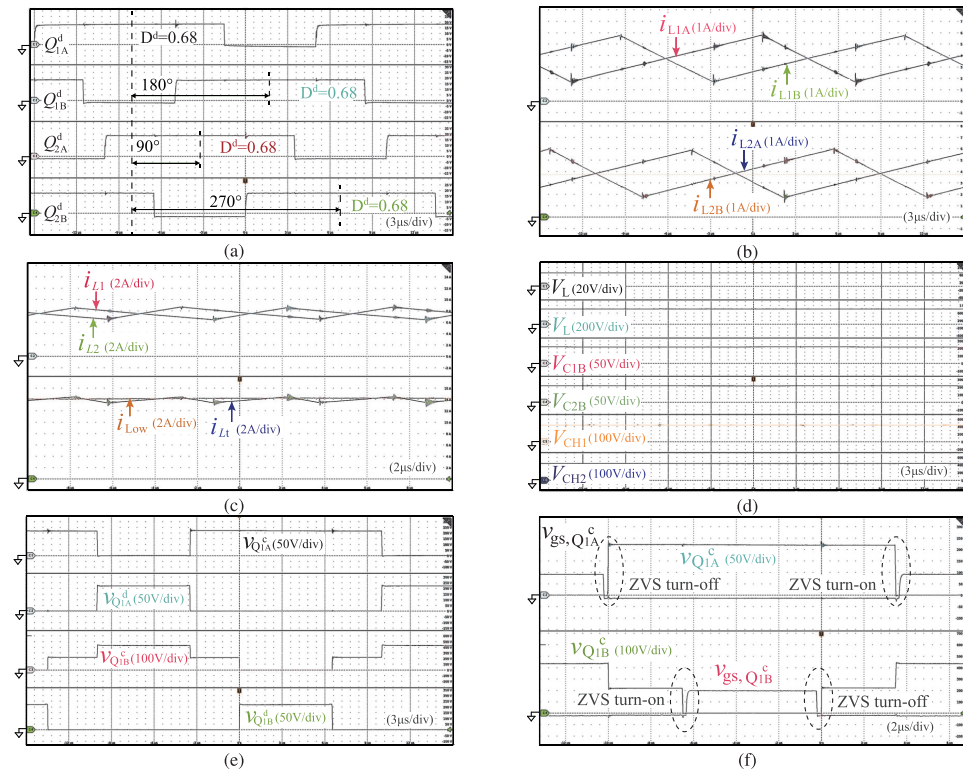


Fig. 20. Observed waveforms in a boost mode with $V_L = 72$ V and $R_H = 640$ Ω for $V_H = 800$ V: (a) gate signals, (b) DC inductor currents, (c) high and low-side unit DC inductor currents and the input currents, (d) capacitor voltages, (e) power switch voltage stresses, and (f) synchronous rectifier voltages.

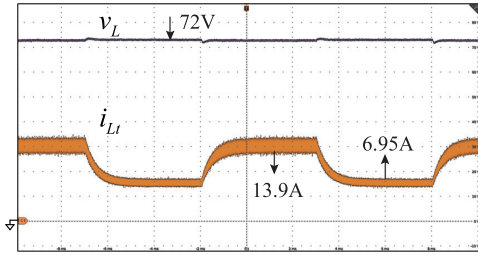


Fig. 21. Transient waveforms of the inductor current and output voltage in the buck mode (10 V/div, 5 A/div, 2 ms/div).

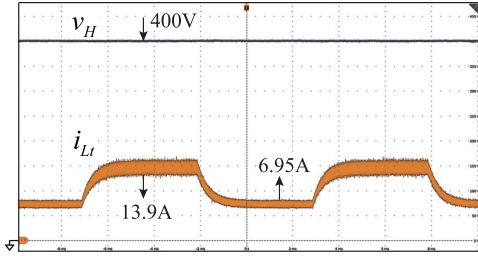


Fig. 22. Transient waveforms of the inductor current and output voltage in the boost mode (50 V/div, 5 A/div, 2 ms/div).

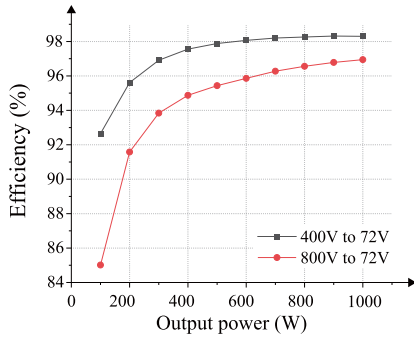


Fig. 23. Actual efficiencies in a buck mode (measured by YOKOGAWA WT1800 power analyzer).

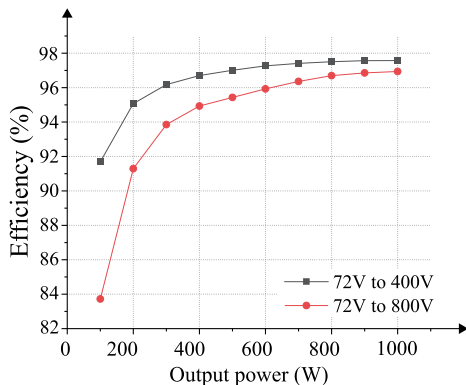


Fig. 24. Actual efficiencies in a boost mode (measured by YOKOGAWA WT1800 power analyzer).

Fig. 17(e) illustrates the steady-state voltage stresses on switches Q_{1A}^c , Q_{1A}^d , Q_{1B}^c , and Q_{1B}^d , whereby $V_{Q_{1A}^c} = 141.3$ V, $V_{Q_{1A}^d} = 142.1$ V, $V_{Q_{1B}^c} = 236.1$ V, and $V_{Q_{1B}^d} = 235.8$ V are lower than the high side voltage $V_H = 400$ V. It should be remarked herein some voltage stresses are even lower than half

of V_H . The black dash-circles in Fig. 17(f) reveal the successful achievement of both ZVS turn-ON and turn-OFF on the counterpart switches Q_{1A}^d , Q_{1B}^d under the condition of SR. By substituting the relevant parameters, the critical load resistance for achieving ZVS in the buck mode can be determined to be $R_L = 13.7 \Omega$. It is worthwhile noting that due to the hard-switching operation of the main switches, rapid discharge of the parasitic capacitance C_{oss} inherently occurs at the turn-ON transitions, which leads to the voltage oscillations. Consequently, the voltage oscillations induced by the turn-ON of the main switches will inevitably provoke voltage oscillations upon the turn-OFF of SR switches.

2) 800 V to 72 V: Fig. 18 presents the key experimental waveforms in a buck mode, where the dc input voltage V_H and the load resistance R_L are set at 800 V and 5.184Ω , respectively. It can be observed in Fig. 18(a) that the sequential operations of the main switches Q_{1A}^c , Q_{2A}^c , Q_{1B}^c , and Q_{2B}^c exhibit a phase shift of 90° . In this condition, the A-DLC1 is inactive and the duty cycle for all the main switches is consistently set at 0.34. Fig. 18(b) displays the current waveforms of the dc inductors. The average currents for L_{1A} , L_{1B} , L_{2A} , and L_{2B} are measured as $I_{L_{1A}} = 3.73$ A, $I_{L_{1B}} = 3.69$ A, $I_{L_{2A}} = 3.77$ A, and $I_{L_{2B}} = 3.72$ A, respectively. These values also demonstrate a well-balanced average inductor current. In addition, the current ripples for $i_{L_{1A}}$, $i_{L_{1B}}$, $i_{L_{2A}}$, and $i_{L_{2B}}$ are $\Delta I_{L_{1A}} = 4.12$ A, $\Delta I_{L_{1B}} = 4.07$ A, $\Delta I_{L_{2A}} = 4.18$ A, and $\Delta I_{L_{2B}} = 4.15$ A, respectively, which has good agreement with (17). The current ripple rates for these inductors are found to be 0.55, 0.55, 0.55, and 0.56, respectively, corresponding to the theoretical values in (18). Hence, the validity of the current ripple analysis for duty cycles is clarified in the range of $0 < D^c < 0.5$.

Due to the adoption of interleaved switching topologies, the current ripple rates for i_{L1} , and i_{L2} are further reduced to 0.14 and 0.15, respectively, as shown in Fig. 18(c). Similarly, the total current of the interleaved inductors, i_{Lt} has small current ripple rate, which allows for a reduction in the use of filtering capacitors. Fig. 18(d) shows that the steady-state voltages across the capacitors are $V_{C_{1B}} = 216.9$ V, $V_{C_{2B}} = 217.8$ V, $V_{C_{H1}} = 439.2$ V, $V_{C_{H2}} = 436.9$ V, and $V_H = 800$ V, corresponding well with the theoretical values (11) and (12).

Fig. 18(e) illustrates the steady-state turn-OFF voltage stresses on switches Q_{1A}^c , Q_{1A}^d , Q_{1B}^c , and Q_{1B}^d . The observed values $V_{Q_{1A}^c} = 222.1$ V, $V_{Q_{1A}^d} = 221.0$ V, $V_{Q_{1B}^c} = 431.3$ V, and $V_{Q_{1B}^d} = 220.3$ V are lower than the high voltage $V_H = 800$ V. In addition, the black dash-circles in Fig. 18(f) reveal the successful achievement of both ZVS turn-ON and ZVS turn-OFF commutations on the counterpart switches Q_{1A}^d , Q_{1B}^d under the condition of SR.

B. Steady-State Performances in the Boost Mode

1) 72 V to 400 V: Fig. 19 illustrates the key experimental waveforms in the boost mode, where the dc input voltage V_L and the load resistance R_H are set to 72 V and 160Ω , respectively. It can be observed in Fig. 19(a) that the main switches Q_{1A}^d , Q_{2A}^d , Q_{1B}^d , and Q_{2B}^d are driven in the sequential manner with a phase shift angle of 90° . The duty cycles for Q_{1A}^d , Q_{2A}^d

TABLE V
COMPARISON OF DIFFERENT NONISOLATED BIDIRECTIONAL DC-DC CONVERTERS

Ref.	Peak efficiency		Voltage ratio		Components	Specifications	Maximum device voltage stress		I_L balance
	Boost	Buck	Boost	Buck			Capacitors	MOSFETs	
[27]	97.5%	94.3%	$\frac{1}{(1-D_{\text{boost}})^2}$	D_{buck}^2	L:2; C:3 SW:4	25V/250V 160W/Si 30kHz/PWM	U_{high}	$\frac{(2-D_{\text{boost}})U_{\text{high}}}{1-D_{\text{boost}}}$	D = 0.5
[28]	95.2%	95.3%	$\frac{2}{1-D_{\text{boost}}}$	$\frac{D_{\text{buck}}}{2}$	L:2; C:4 SW:5	50-120V/400V 1kW/Si 20kHz/PWM	$\frac{U_{\text{high}}}{2}$	$\frac{U_{\text{high}}}{2}$	Full duty
[29]	96.4%	96.7%	$\frac{2+D_{\text{boost}}}{1-D_{\text{boost}}}$	$\frac{D_{\text{buck}}}{3-D_{\text{buck}}}$	L:3; C:5 SW:5	40-120V/400V 1kW/Si 50kHz/PWM	U_{high}	$\frac{2(U_{\text{high}}+U_{\text{low}})}{3}$	Full duty
[30]	95.8%	95.9%	$\frac{3}{1-D_{\text{boost}}}$	$\frac{D_{\text{buck}}}{3}$	L:3; C:6 SW:8	30-100V/400V 800W/Si 20kHz/PWM	U_{high}	$\frac{U_{\text{high}}}{3}$	—
[31]	96.5%	96.5%	$\frac{N+2}{N(1-D_{\text{boost}})}$	—	L:2; CL:1; C:4 SW:6	40-60V/400V 1kW/Si 50kHz/PWM	$\frac{NU_{\text{high}}}{N+2}$	$\frac{2U_{\text{high}}}{N+2}$	Full duty
[32]	96.1%	96.6%	$\frac{2N+2}{1-D_{\text{boost}}}$	$\frac{D_{\text{buck}}}{2N+2}$	CL:3; C:6 SW:6	48V/380V 250W/Si 50kHz/PWM	U_{high}	—	Full duty
[33]	96%	96%	$\frac{2N+2}{1-D_{\text{boost}}}$	$\frac{D_{\text{buck}}}{2N+2}$	CL:2; C:6 SW:8	30-40V/400V 1kW/Si 50kHz/PWM	U_{high}	$\frac{NU_{\text{high}}}{N+1}$	Full duty
[34]	95.7%	95.4%	$\frac{4N}{4D_{\text{boost}}+1}+2$	—	BT:2; L:2; C:3 SW:8	40-60V/400V 1kW/Si 50kHz/PWM	—	—	Full duty
[35]	96.8%	96.8%	$\frac{N+2}{N(1-D_{\text{boost}})}$	—	L:2; CL:1; C:6 SW:8; D:2	40-60V/400V 1kW/Si 50kHz/PWM	U_{high}	$\frac{U_{\text{high}}}{N+2}$	Full duty
[36]	97.5%	97.5%	$\frac{2}{1-D_{\text{boost}}}$	$\frac{D_{\text{buck}}}{2}$	L:2; C:3 SW:4	60V/200-380V 500W/SiC 50kHz/PWM	U_{high}	U_{high}	Full duty
Prop.	97.6%	98.3%	$\frac{3+D_{\text{boost}}}{1-D_{\text{boost}}}$	$\frac{D_{\text{buck}}}{4-D_{\text{buck}}}$	L:4; C:5 SW:8	72V/400-800V 1kW/SiC 50kHz/PWM	$\frac{U_{\text{high}}+U_{\text{low}}}{2}$	$\frac{U_{\text{high}}+U_{\text{low}}}{2}$	Full duty

N: Turns ratio; L: Inductor; CL: Coupled inductor; C: Capacitor; BT: Built-in transformer; SW: Power switch; D: Diode; —: Not reported.

are consistently fixed at 0.5, while those for Q_{1B}^d and Q_{2B}^d are set at 0.41. The current waveforms of the dc inductors are depicted in Fig. 19(b). The average currents through L_{1A} , L_{1B} , L_{2A} , and L_{2B} , are obtained as $I_{L_{1A}} = 4.04$ A, $I_{L_{1B}} = 4.10$ A, $I_{L_{2A}} = 4.07$ A, and $I_{L_{2B}} = 4.11$ A, respectively, which implies that a well-balanced average inductor current can be achieved in the proposed converter with the A-DLC2. The current ripples for $i_{L_{1A}}$, $i_{L_{1B}}$, $i_{L_{2A}}$, and $i_{L_{2B}}$ are $\Delta I_{L_{1A}} = 3.12$ A, $\Delta I_{L_{1B}} = 2.61$ A, $\Delta I_{L_{2A}} = 3.10$ A, and $\Delta I_{L_{2B}} = 2.67$ A, respectively, which has good agreement with (23) and (24). The current ripple rates for these inductors are found to be 0.39, 0.32, 0.38, and 0.32, respectively, corresponding to the theoretical analyses in (25) and (26). Thus, the validity of the current ripple analysis for duty cycles in the range of $0 < D^d \leq 0.5$ is verified herein.

As shown in Fig. 19(c), the current ripple rates for i_{L_1} , and i_{L_2} are further reduced to 0.13 and 0.14, respectively, due to the adoption of interleaved switching patterns. Fig. 19(d) presents the steady-state voltages across the capacitors. The measured values $V_{C_{1B}} = 94.7$ V, $V_{C_{2B}} = 93.9$ V, $V_{C_{H1}} = 235.9$ V, $V_{C_{H2}} = 232.7$ V, and $V_L = 72$ V correspond well with (14) and (15). In addition, the output voltage is recorded as $V_H = 400$ V, whereby the validity of (10) is revealed.

Fig. 19(e) illustrates the voltage stresses on switches Q_{1A}^c , Q_{1B}^c , and Q_{2B}^c . The observed steady-state turn-OFF

values $V_{Q_{1A}^c} = 143.5$ V, $V_{Q_{1B}^c} = 140.8$ V, $V_{Q_{2B}^c} = 238.2$ V, and $V_{Q_{1B}^d} = 237.6$ V are lower than $V_H = 400$ V. It should be remarked herein that some voltage stresses are even lower than half of V_H . Furthermore, the black dash-circles in Fig. 19(f) reveal the successful achievement of both the ZVS turn-ON and ZVS turn-OFF commutations on the counterpart switches Q_{1A}^c , Q_{1B}^c under the condition of SR. Accordingly, the critical resistance of ZVS in the boost mode can be determined as $R_H = 411.5 \Omega$ for the output voltage of 400 V.

2) 72 V to 800 V: Fig. 20 displays the critical experimental waveforms in a boost mode, where the dc input voltage V_L and the load resistance R_H are set at 72 V and 640 Ω , respectively. It can be observed in Fig. 20(a) that the sequential operations of the main switches Q_{1A}^d , Q_{2A}^d , Q_{1B}^d , and Q_{2B}^d exhibit a phase shift of 90°. During this period, the A-DLC2 is inactive and the duty cycle for all the main switches is set at 0.68. The current waveforms of the inductors are shown in Fig. 20(b). The average currents for L_{1A} , L_{1B} , L_{2A} , and L_{2B} , are measured as $I_{L_{1A}} = 3.79$ A, $I_{L_{1B}} = 3.86$ A, $I_{L_{2A}} = 3.81$ A, and $I_{L_{2B}} = 3.83$ A, respectively. Thus, the average inductor currents are well-balanced in the proposed BDC. The current ripples for $i_{L_{1A}}$, $i_{L_{1B}}$, $i_{L_{2A}}$, and $i_{L_{2B}}$ are $\Delta I_{L_{1A}} = 4.13$ A, $\Delta I_{L_{1B}} = 4.10$ A, $\Delta I_{L_{2A}} = 4.14$ A, and $\Delta I_{L_{2B}} = 4.17$ A, respectively, which has good agreement with (27). The current ripple rates for these inductors are found

as 0.54, 0.53, 0.54, and 0.55, respectively, which agree well with the theoretical values in (28). These results validate the precision of the current ripple analysis for duty cycles in the range of $0.5 < D^d < 1$.

Due to the interleaved switching patterns, the current ripple rates for i_{L1} , and i_{L2} are further reduced to 0.14 and 0.15, respectively, as shown in Fig. 20(c). Fig. 20(d) shows that the steady-state voltages across the capacitors are $V_{C_{1B}} = 217.5$ V, $V_{C_{2B}} = 218.8$ V, $V_{C_{H1}} = 438.3$ V, $V_{C_{H2}} = 436.8$ V, and $V_L = 72$ V, corresponding well with (14) and (15). The output voltage is obtained as $V_H = 800$ V.

Fig. 20(e) illustrates the voltage stresses on Q_{1A}^c , Q_{1A}^d , Q_{1B}^c , and Q_{1B}^d . The steady-state turn-OFF voltages are observed as $V_{Q_{1A}^c} = 223.9$ V, $V_{Q_{1A}^d} = 225.7$ V, $V_{Q_{1B}^c} = 436.8$ V, and $V_{Q_{1B}^d} = 222.4$ V. It should be remarked herein that voltage stresses of a few power devices are even lower than half of V_H . In addition, the successful achievements of both the ZVS turn-ON and ZVS turn-OFF commutations on the counterpart switches Q_{1A}^c , Q_{1B}^c are observed under the condition of SR in Fig. 20(f). The critical resistance of ZVS for the output voltage of 800 V can be determined as $R_H = 890.5$ Ω .

C. Dynamic Performances

Fig. 21 illustrates the waveforms of inductor current i_{Lt} and output voltage V_L in a buck mode where the input voltage is fixed at $V_H = 400$ V but the load resistance periodically exchanges between 5.18 Ω for 1 kW to 10.36 Ω (500 W). It is evident from the transitional performances that V_L is regulated at 72 V regardless of the load variations.

In a similar way, Fig. 22 depicts the waveforms of inductor current i_{Lt} and output voltage in the boost mode, when the input voltage is $V_H = 72$ V, and the load resistance periodically varies from 160 Ω (1 kW) to 320 Ω (500 W). It is evident from the dynamical waveforms that the output voltage V_H is well controlled at 400 V while the load resistance exchanges between the two sets of values.

D. Power Conversion Efficiencies

The actual efficiencies of the F4P-ICPBDC with the A-DLC is evaluated for the buck / boost modes by the closed-loop controller scheme with two sets of V_H : 400 V and 800 V. As displayed in Fig. 23, the maximum efficiencies are recorded as 98.3% and 96.9% for $V_H = 400$ V and 800 V, respectively, in the buck mode. The maximum efficiencies are 97.6% and 96.9%, respectively, for $V_H = 400$ V and 800 V in the boost mode, as indicated in Fig. 24. Therefore, the high efficiencies of the proposed F4P-ICPBDC are actually verified in both the power flows. In particular, over 98% efficiency attains in the 60%–100% load ratios of the buck mode (400 V to 72 V).

E. Comparison With Existing BDCs

In order to reveal the performance of the proposed BDC, a comprehensive comparison with the existing BDC topologies

from the literatures [27], [28], [29], [30], [31], [32], [33], [34], [35], [36], are summarized in Table V as well as the descriptions in Section I. The higher voltage ratio and higher efficiency can be attained by the proposed BDC while the counts of the magnetic components are relatively high. The passive components can be reduced by adopting the magnetic integration of the dc inductors. Employment of SiC-MOSFETs is dedicated to achieving the high efficiency despite eight active switches in the four-phase structure.

The characteristics of SiC-MOSFETs, i.e., faster switching speeds and the lower ON-resistance contribute to reduction of switching losses and promotion of overall efficiency of converter even with hard switching. Besides, the efficiency is further optimized by the proposed BDC, due to Zero-Voltage Switching (ZVS) achievable in the SR switches. In addition, 800 V dc voltage in the input or output side is shared by two active switches in the proposed BDC. Accordingly, 650 V-class SiC-MOSFET is irreplaceable for the F4P-ICPBDC topology.

VI. CONCLUSION

The F4P-ICPBDC topology has been proposed in this article, and its operating principle and the excellent performance have been demonstrated in addition to the sound amount of steady-state analysis and design guideline of the circuit parameters. The essential performance of the proposed BDC have been investigated by experiments including the enhanced voltage ratio, high efficiency as well as the current balances in the dc inductors.

The wide buck/boost voltage ratios and full-range inherent current balancing properties can be attained by the proposed circuit topology and duty cycle control scheme. The asymmetrical DLC strategy has been demonstrated for an EV-DCMGs system with a wide range high-side voltage. A prototype with SiC-MOSFETs has been developed with a specification of 1 kW–50 kHz to reveal the actual performance of F4P-ICPBDC, whereby a wide voltage ratio range between the variable high-side voltage (400–800 V) and the constant low-side voltage (72 V) have been actually verified. The prototype can achieve maximum efficiencies above 98.3%. By comparing to the existing BDCs, the higher efficiency and higher voltage ratio can attain due to the SiC-MOSFET based the F4P-ICPBDC topology.

Future research will include implementing soft switching for all main switches and adopting integrated inductors. Then, enhancing the operating frequency and increasing power density will be pursued for a wide variety of BDC applications.

APPENDIX

The average models of the converter are derived by utilizing the state-space averaging method in order to facilitate the steady-state performance of the proposed BDC. In the buck mode, C_{H1} , C_{H2} , and C_L are connected in series while in parallel with the high-voltage side dc source. Therefore, an equivalent series resistance (e.g., $r = 0.2$ Ω) for the dc source is considered

to prevent invalid state variables. Referring to Figs. 5(a) and 6, the state equations corresponding to each mode can be obtained when $D^c < 0.5$. By combining these state equations, the average model can be described in a matrix form as expressed by (44), shown at the bottom of this page. Similarly, referring to Figs. 5(b) and 6, the state equations corresponding to each mode can be obtained when $D^c \geq 0.5$. By combining these state equations, the average model can be derived in a matrix form as expressed by (45), shown at the bottom of this page.

In the boost mode, the state equations corresponding to each mode can be derived when $D^d \leq 0.5$ by referring to Figs. 8(a) and 9. By utilizing these state equations, the average model can be derived in matrix form as written by (46), shown at the bottom of this page. Similarly, referring to Figs. 8(b) and 9, the state equations corresponding to each mode can be obtained when $D^d > 0.5$. Then, based on these state equations, the average model can be derived in a matrix form as denoted by (47), shown at the top of the next page.

$$\frac{d}{dt} \begin{bmatrix} i_{L_{1A}}(t) \\ i_{L_{1B}}(t) \\ i_{L_{2A}}(t) \\ i_{L_{2B}}(t) \\ u_{C_{1B}}(t) \\ u_{C_{2B}}(t) \\ u_{C_{H1}}(t) \\ u_{C_{H2}}(t) \\ u_{C_L}(t) \end{bmatrix} = \begin{bmatrix} 0 & 0 & 0 & 0 & \frac{D^c}{L_{1A}} & 0 & \frac{D^c}{L_{1A}} & 0 & \frac{-1}{L_{1A}} \\ 0 & 0 & 0 & 0 & \frac{D^c}{L_{1B}} & 0 & 0 & 0 & \frac{-1}{L_{1B}} \\ 0 & 0 & 0 & 0 & 0 & \frac{-D^c}{L_{2A}} & 0 & \frac{D^c}{L_{2A}} & \frac{-1}{L_{2A}} \\ 0 & 0 & 0 & 0 & 0 & \frac{D^c}{L_{2B}} & 0 & 0 & \frac{-1}{L_{2B}} \\ \frac{D^c}{C_{1B}} & \frac{-D^c}{C_{1B}} & 0 & 0 & 0 & 0 & 0 & 0 & 0 \\ 0 & 0 & \frac{D^c}{C_{2B}} & \frac{-D^c}{C_{2B}} & 0 & 0 & 0 & 0 & 0 \\ \frac{-D^c}{C_{H1}} & 0 & 0 & 0 & 0 & 0 & \frac{-1}{C_{H1}r} & \frac{-1}{C_{H1}r} & \frac{1}{C_{H1}r} \\ 0 & 0 & \frac{-D^c}{C_{H2}} & 0 & 0 & 0 & \frac{-1}{C_{H2}r} & \frac{-1}{C_{H2}r} & \frac{1}{C_{H2}r} \\ \frac{1}{C_L} & \frac{1}{C_L} & \frac{1}{C_L} & \frac{1}{C_L} & 0 & 0 & \frac{-1}{C_L r} & \frac{-1}{C_L r} & \frac{1}{C_L r} - \frac{1}{R_L C_L} \end{bmatrix} \begin{bmatrix} i_{L_{1A}}(t) \\ i_{L_{1B}}(t) \\ i_{L_{2A}}(t) \\ i_{L_{2B}}(t) \\ u_{C_{1B}}(t) \\ u_{C_{2B}}(t) \\ u_{C_{H1}}(t) \\ u_{C_{H2}}(t) \\ u_{C_L}(t) \end{bmatrix} + \begin{bmatrix} 0 \\ 0 \\ 0 \\ 0 \\ 0 \\ 0 \\ \frac{1}{C_{H1}r} \\ \frac{1}{C_{H2}r} \\ \frac{1}{C_L r} \end{bmatrix} u_H(t) \quad (44)$$

$$\frac{d}{dt} \begin{bmatrix} i_{L_{1A}}(t) \\ i_{L_{1B}}(t) \\ i_{L_{2A}}(t) \\ i_{L_{2B}}(t) \\ u_{C_{1B}}(t) \\ u_{C_{2B}}(t) \\ u_{C_{H1}}(t) \\ u_{C_{H2}}(t) \\ u_{C_L}(t) \end{bmatrix} = \begin{bmatrix} 0 & 0 & 0 & 0 & \frac{-1}{2L_{1A}} & 0 & \frac{1}{2L_{1A}} & 0 & \frac{-1}{L_{1A}} \\ 0 & 0 & 0 & 0 & \frac{1}{2L_{1B}} & 0 & \frac{2D^c-1}{2L_{1B}} & 0 & \frac{-1}{L_{1B}} \\ 0 & 0 & 0 & 0 & 0 & \frac{-1}{2L_{2A}} & 0 & \frac{1}{2L_{2A}} & \frac{-1}{L_{2A}} \\ 0 & 0 & 0 & 0 & 0 & \frac{1}{2L_{2B}} & 0 & \frac{2D^c-1}{2L_{2B}} & \frac{-1}{L_{2B}} \\ \frac{1}{2C_{1B}} & \frac{-1}{2C_{1B}} & 0 & 0 & 0 & 0 & 0 & 0 & 0 \\ 0 & 0 & \frac{1}{2C_{2B}} & \frac{-1}{2C_{2B}} & 0 & 0 & 0 & 0 & 0 \\ \frac{-1}{2C_{H1}} & \frac{2D^c-1}{2C_{H1}} & 0 & 0 & 0 & 0 & \frac{-1}{C_{H1}r} & \frac{-1}{C_{H1}r} & \frac{1}{C_{H1}r} \\ 0 & 0 & \frac{-1}{2C_{H2}} & \frac{-2D^c-1}{2C_{H2}} & 0 & 0 & \frac{-1}{C_{H2}r} & \frac{-1}{C_{H2}r} & \frac{1}{C_{H2}r} \\ \frac{1}{C_L} & \frac{1}{C_L} & \frac{1}{C_L} & \frac{1}{C_L} & 0 & 0 & \frac{-1}{C_L r} & \frac{-1}{C_L r} & \frac{R_L-r}{C_L R_L C_L r} \end{bmatrix} \begin{bmatrix} i_{L_{1A}}(t) \\ i_{L_{1B}}(t) \\ i_{L_{2A}}(t) \\ i_{L_{2B}}(t) \\ u_{C_{1B}}(t) \\ u_{C_{2B}}(t) \\ u_{C_{H1}}(t) \\ u_{C_{H2}}(t) \\ u_{C_L}(t) \end{bmatrix} + \begin{bmatrix} 0 \\ 0 \\ 0 \\ 0 \\ 0 \\ 0 \\ \frac{1}{C_{H1}r} \\ \frac{1}{C_{H2}r} \\ \frac{1}{C_L r} \end{bmatrix} u_H(t) \quad (45)$$

$$\left\{ \begin{array}{l} \frac{d}{dt} \begin{bmatrix} i_{L_{1A}}(t) \\ i_{L_{1B}}(t) \\ i_{L_{2A}}(t) \\ i_{L_{2B}}(t) \\ u_{C_{1B}}(t) \\ u_{C_{2B}}(t) \\ u_{C_{H1}}(t) \\ u_{C_{H2}}(t) \end{bmatrix} = \begin{bmatrix} 0 & 0 & 0 & 0 & \frac{1}{2L_{1A}} & 0 & \frac{-1}{2L_{1A}} & 0 \\ 0 & 0 & 0 & 0 & \frac{-1}{2L_{1B}} & 0 & \frac{2D^d-1}{2L_{1B}} & 0 \\ 0 & 0 & 0 & 0 & 0 & \frac{1}{2L_{2A}} & 0 & \frac{-1}{2L_{2A}} \\ 0 & 0 & 0 & 0 & 0 & \frac{-1}{2L_{2B}} & 0 & \frac{2D^d-1}{2L_{2B}} \\ \frac{-1}{2C_{1B}} & \frac{1}{2C_{1B}} & 0 & 0 & 0 & 0 & 0 & 0 \\ 0 & 0 & \frac{-1}{2C_{2B}} & \frac{1}{2C_{1B}} & 0 & 0 & 0 & 0 \\ \frac{1}{2C_{H1}} & \frac{1-2D^d}{2C_{H1}} & 0 & 0 & 0 & 0 & \frac{-1}{C_{H1}R_H} & \frac{-1}{C_{H1}R_H} \\ 0 & 0 & \frac{1}{2C_{H2}} & \frac{1-2D^d}{2C_{H2}} & 0 & 0 & \frac{-1}{C_{H2}R_H} & \frac{-1}{C_{H2}R_H} \end{bmatrix} \begin{bmatrix} i_{L_{1A}}(t) \\ i_{L_{1B}}(t) \\ i_{L_{2A}}(t) \\ i_{L_{2B}}(t) \\ u_{C_{1B}}(t) \\ u_{C_{2B}}(t) \\ u_{C_{H1}}(t) \\ u_{C_{H2}}(t) \end{bmatrix} + \begin{bmatrix} \frac{1}{L_{1A}} \\ \frac{1}{L_{1B}} \\ \frac{1}{L_{2A}} \\ \frac{1}{L_{2B}} \\ 0 \\ 0 \\ \frac{1}{C_{H1}R_H} \\ \frac{1}{C_{H2}R_H} \end{bmatrix} u_L(t) \\ u_H = u_{C_{H1}} + u_{C_{H2}} - u_L \end{array} \right. \quad (46)$$

$$\left\{ \begin{array}{l} \frac{d}{dt} \begin{bmatrix} i_{L_{1A}}(t) \\ i_{L_{1B}}(t) \\ i_{L_{2A}}(t) \\ i_{L_{2B}}(t) \\ u_{C_{1B}}(t) \\ u_{C_{2B}}(t) \\ u_{C_{H1}}(t) \\ u_{C_{H2}}(t) \end{bmatrix} \\ u_H = u_{C_{H1}} + u_{C_{H2}} - u_L \end{array} \right. = \begin{bmatrix} 0 & 0 & 0 & 0 & \frac{1-D^d}{L_{1A}} & 0 & \frac{D^d-1}{L_{1A}} & 0 \\ 0 & 0 & 0 & 0 & \frac{D^d-1}{L_{1B}} & 0 & 0 & 0 \\ 0 & 0 & 0 & 0 & 0 & \frac{1-D^d}{L_{2A}} & 0 & \frac{D^d-1}{L_{2A}} \\ 0 & 0 & 0 & 0 & 0 & \frac{D^d-1}{L_{2B}} & 0 & 0 \\ \frac{D^d-1}{C_{1B}} & \frac{1-D^d}{C_{1B}} & 0 & 0 & 0 & 0 & 0 & 0 \\ 0 & 0 & \frac{D^d-1}{C_{2B}} & \frac{1-D^d}{C_{1B}} & 0 & 0 & 0 & 0 \\ \frac{1-D^d}{C_{H1}} & 0 & 0 & 0 & 0 & 0 & \frac{-1}{C_{H1}R_H} & \frac{-1}{C_{H1}R_H} \\ 0 & 0 & \frac{1-D^d}{C_{H2}} & 0 & 0 & 0 & \frac{-1}{C_{H2}R_H} & \frac{-1}{C_{H2}R_H} \end{bmatrix} \begin{bmatrix} i_{L_{1A}}(t) \\ i_{L_{1B}}(t) \\ i_{L_{2A}}(t) \\ i_{L_{2B}}(t) \\ u_{C_{1B}}(t) \\ u_{C_{2B}}(t) \\ u_{C_{H1}}(t) \\ u_{C_{H2}}(t) \end{bmatrix} + \begin{bmatrix} \frac{1}{L_{1A}} \\ \frac{1}{L_{1B}} \\ \frac{1}{L_{2A}} \\ \frac{1}{L_{2B}} \\ 0 \\ 0 \\ 0 \\ \frac{1}{C_{H1}R_H} \\ \frac{1}{C_{H2}R_H} \end{bmatrix} u_L(t) \quad (47)$$

REFERENCES

- [1] M. Yilmaz and P. T. Krein, "Review of battery charger topologies, charging power levels, and infrastructure for plug-in electric and hybrid vehicles," *IEEE Trans. Power Electron.*, vol. 28, no. 5, pp. 2151–2169, May 2013.
- [2] K. Sun, L. Zhang, Y. Xing, and J. M. Guerrero, "A distributed control strategy based on DC bus signaling for modular photovoltaic generation systems with battery energy storage," *IEEE Trans. Power Electron.*, vol. 26, no. 10, pp. 3032–3045, Oct. 2011.
- [3] S. Semsar, T. Soong, and P. W. Lehn, "On-board single-phase integrated electric vehicle charger with V2G functionality," *IEEE Trans. Power Electron.*, vol. 35, no. 11, pp. 12072–12084, Nov. 2020.
- [4] H. J. Raherimihaja, Q. Zhang, G. Xu, and X. Zhang, "Integration of battery charging process for EVs into segmented three-phase motor drive with V2G-mode capability," *IEEE Trans. Ind. Electron.*, vol. 68, no. 4, pp. 2834–2844, Apr. 2021.
- [5] I.-O. Lee, "Hybrid PWM-resonant converter for electric vehicle on-board battery chargers," *IEEE Trans. Power Electron.*, vol. 31, no. 5, pp. 3639–3649, May 2016.
- [6] M. Kwon and S. Choi, "An electrolytic capacitorless bidirectional EV charger for V2G and V2H applications," *IEEE Trans. Power Electron.*, vol. 32, no. 9, pp. 6792–6799, Sep. 2017.
- [7] V. T. Tran, M. R. Islam, K. M. Muttaqi, O. Farrok, M. R. Kiran, and D. Sutanto, "A novel universal magnetic power plug to facilitate V2V/V2G/G2V/V2H connectivity for future grid infrastructure," *IEEE Trans. Ind. Appl.*, vol. 58, no. 1, pp. 951–961, Jan./Feb. 2022.
- [8] K.-W. Hu and C.-M. Liaw, "Incorporated operation control of DC microgrid and electric vehicle," *IEEE Trans. Ind. Electron.*, vol. 63, no. 1, pp. 202–215, Jan. 2016.
- [9] Y. Xuan, X. Yang, W. Chen, T. Liu, and X. Hao, "A novel three-level CLLC resonant dc-dc converter for bidirectional EV charger in dc microgrids," *IEEE Trans. Ind. Electron.*, vol. 68, no. 3, pp. 2334–2344, Mar. 2021.
- [10] M. Wang, S. Tan, C. Lee, and S. Y. Hui, "A configuration of storage system for DC microgrids," *IEEE Trans. Power Electron.*, vol. 33, no. 5, pp. 3722–3733, May 2018.
- [11] W. Li, C. Xu, H. Yu, Y. Gu, and X. He, "Analysis, design and implementation of isolated bidirectional converter with winding-cross-coupled inductors for high step-up and high step-down conversion system," *IET Power Electron.*, vol. 7, no. 1, pp. 67–77, Jan. 2014.
- [12] B. Long, W. Zeng, J. Rodríguez, J. M. Guerrero, J. Hu, and K. T. Chong, "Enhancement of voltage regulation capability for DC-microgrid composed by battery test system: A fractional-order virtual inertia method," *IEEE Trans. Power Electron.*, vol. 37, no. 10, pp. 12538–12551, Oct. 2022.
- [13] L. Zheng et al., "SiC-based 5-kV universal modular soft-switching solid-state transformer (M-S4T) for medium-voltage DC microgrids and distribution grids," *IEEE Trans. Power Electron.*, vol. 36, no. 10, pp. 11326–11343, Oct. 2021.
- [14] W. C. Leal, M. O. Godinho, R. F. Bastos, C. R. de Aguiar, G. H. F. Fuzato, and R. Q. Machado, "Cascaded interleaved DC-DC converter for a bidirectional electric vehicle charging station," *IEEE Trans. Ind. Electron.*, vol. 71, no. 4, pp. 3708–3717, Apr. 2024.
- [15] C. M. Lai, C. T. Pan, and M. C. Cheng, "High-efficiency modular high step-up interleaved boost converter for DC-microgrid applications," *IEEE Trans. Ind. Appl.*, vol. 48, no. 1, pp. 161–171, Jan./Feb. 2012.
- [16] T. F. Wu, Y. C. Chen, J. G. Yang, and C. L. Kuo, "Isolated bidirectional full-bridge DC-DC converter with a flyback snubber," *IEEE Trans. Power Electron.*, vol. 25, no. 7, pp. 1915–1922, Jul. 2010.
- [17] G. Chen, Y. S. Lee, S. Y. R. Hui, D. Xu, and Y. Wang, "Actively clamped bidirectional flyback converter," *IEEE Trans. Ind. Electron.*, vol. 47, no. 4, pp. 770–779, Aug. 2000.
- [18] A. Rodríguez, A. Vazquez, D. G. Lamar, M. M. Hernando, and J. Sebastian, "Different purpose design strategies and techniques to improve the performance of a dual active bridge with phase-shift control," *IEEE Trans. Power Electron.*, vol. 30, no. 2, pp. 790–804, Feb. 2015.
- [19] K. Jin, M. Yang, X. Ruan, and M. Xu, "Three-level bidirectional converter for fuel-cell/battery hybrid power system," *IEEE Trans. Ind. Electron.*, vol. 57, no. 6, pp. 1976–1986, Jun. 2010.
- [20] P. Das, S. A. Mousavi, and G. Moschopoulos, "Analysis, design, and control of a nonisolated bidirectional ZVS-PWM DC-DC converter with coupled inductors," *IEEE Trans. Power Electron.*, vol. 25, no. 10, pp. 2630–2641, Oct. 2010.
- [21] S. B. Santra, D. Chatterjee, and Y. P. Siwakoti, "Coupled inductor based soft switched high gain bidirectional DC-DC converter with reduced input current ripple," *IEEE Trans. Ind. Electron.*, vol. 70, no. 2, pp. 1431–1443, Feb. 2023.
- [22] S. Busquets-Monge, S. Alepuz, and J. Bordonau, "A bidirectional multi-level boost-buck DC-DC converter," *IEEE Trans. Power Electron.*, vol. 26, no. 8, pp. 2172–2183, Aug. 2011.
- [23] J. Roy and R. Ayyanar, "Sensor-less current sharing over wide operating range for extended-duty-ratio boost converter," *IEEE Trans. Power Electron.*, vol. 32, no. 11, pp. 8763–8777, Nov. 2017.
- [24] K. Zou, M. J. Scott, and J. Wang, "A switched-capacitor voltage tripler with automatic interleaving capability," *IEEE Trans. Power Electron.*, vol. 27, no. 6, pp. 2857–2868, Jun. 2012.
- [25] O. Kirshenboim and M. M. Peretz, "High-efficiency nonisolated converter with very high step-down conversion ratio," *IEEE Trans. Power Electron.*, vol. 32, no. 5, pp. 3683–3690, May 2017.
- [26] C. Y. Li, T. H. Chen, and H. C. Chen, "A simple control strategy extending intrinsic current balancing characteristics to achieve a full operating range for interleaved voltage-doubler boost DC-DC converters," *IEEE Trans. Ind. Appl.*, vol. 56, no. 1, pp. 436–445, Jan./Feb., 2020.
- [27] H. Ardi, A. Ajami, F. Kardan, and S. N. Avilagh, "Analysis and implementation of a nonisolated bidirectional DC-DC converter with high voltage gain," *IEEE Trans. Ind. Electron.*, vol. 63, no. 8, pp. 4878–4888, Aug. 2016.
- [28] Y. Zhang, Y. Gao, J. Li, and M. Sumner, "Interleaved switched-capacitor bidirectional DC-DC converter with wide voltage-gain range for energy storage systems," *IEEE Trans. Power Electron.*, vol. 33, no. 5, pp. 3852–3869, May 2018.
- [29] Z. Wang, P. Wang, B. Li, X. Ma, and P. Wang, "A bidirectional DC-DC converter with high voltage conversion ratio and zero ripple current for battery energy storage system," *IEEE Trans. Power Electron.*, vol. 36, no. 7, pp. 8012–8027, Jul. 2021.

- [30] Y. Zhang, W. Zhang, F. Gao, S. Gao, and D. J. Rogers, "A switched-capacitor interleaved bidirectional converter with wide voltage-gain range for super capacitors in EVs," *IEEE Trans. Power Electron.*, vol. 35, no. 2, pp. 1536–1547, Feb. 2020.
- [31] Z. Yan, J. Zeng, W. Lin, and J. Liu, "A novel interleaved nonisolated bidirectional DC-DC converter with high voltage-gain and full-range ZVS," *IEEE Trans. Power Electron.*, vol. 35, no. 7, pp. 7191–7203, Jul. 2020.
- [32] S. B. Santra, D. Chatterjee, and T.-J. Liang, "High gain and high-efficiency bidirectional DC-DC converter with current sharing characteristics using coupled inductor," *IEEE Trans. Power Electron.*, vol. 36, no. 11, pp. 12819–12833, Nov. 2021.
- [33] R. Hu, H. Qi, Z. Yan, W. Wu, J. Zeng, and J. Liu, "A coupled-inductor-based bidirectional DC-DC converter with high voltage conversion ratio and sensorless current balance," *IEEE Trans. Ind. Electron.*, vol. 70, no. 3, pp. 2450–2460, Mar. 2023.
- [34] Z. Yan et al., "Ripple-free bidirectional DC-DC converter with wide ZVS range for battery charging/discharging system," *IEEE Trans. Ind. Electron.*, vol. 70, no. 10, pp. 9992–10002, Oct. 2023.
- [35] Z. Yan, J. Zeng, Z. Guo, R. Hu, and J. Liu, "A soft-switching bidirectional DC-DC converter with high voltage gain and low voltage stress for energy storage systems," *IEEE Trans. Ind. Electron.*, vol. 68, no. 8, pp. 6871–6880, Aug. 2021.
- [36] C.-M. Lai, W.-H. Lin, H.-E. Liu, S. Liu, T. Mishima, and J. Teh, "A two-phase interleaved bidirectional DC-DC converter with asymmetrical duty limit control for wide-range DC-bus voltage applications," *IEEE Trans. Ind. Appl.*, vol. 60, no. 2, pp. 3306–3321, Mar./Apr. 2024.



Shiqiang Liu (Student Member, IEEE) was born in Henan, China, in 1995. He received the B.S. degree in electrical engineering and automation from the Shandong University of Technology, Zibo, China, in 2017, and the M.S. degree in electrical engineering from the Dalian University of Technology, Dalian, China, in 2020. He is currently working toward the Ph.D. degree in electrical engineering with the Faculty of Maritime Sciences, Kobe University, Kobe City, Japan.

His research interests include bidirectional dc–dc converters, HEV/EV onboard chargers, induction heating (IH) systems, EV-connected dc-microgrids (EV-DCMGs) systems, and artificial intelligence applications in power electronics.



Guiyi Dong (Student Member, IEEE) was born in Shandong, China, in 1996. He received the B.S. degree from the School of Information and Electrical Engineering, Shandong Jianzhu University, Shandong, China, and the M.S. degree from Graduate School of Science and Technology, Gunma University, Maebashi, Japan. He is currently working toward the Ph.D. degree in electrical engineering with the Faculty of Maritime Sciences, Kobe University, Kobe, Japan.

His research interests include resonant converters, high-frequency inverters, bidirectional dc–dc converters, bidirectional wireless power transfer (WPT) device for vehicle-to-house (V2H) systems, and the development of high-frequency inverters for WPT and induction heating (IH) systems, with a particular emphasis on the application of direct ac–ac converters.



Tomokazu Mishima (Senior Member, IEEE) received the Ph.D. degree in electrical engineering from The University of Tokushima, Tokushima, Japan, in 2004.

Since 2010, he has been an Associate Professor with Kobe University, Hyogo, Japan, and engages in the researches and developments of power electronics circuits and systems. He has been appointed to the Center for Advanced Medical Engineering Research and Development (CAMED) in 2020, and the research center for Hydrogen Energy Technology (HyTec) in 2024, Kobe University. His research interests include soft-switching dc–dc converters, resonant converters, and high frequency inverters for industrial, automotive, biomedical, renewable, and sustainable energy applications.

Dr. Mishima is the recipient of 2022 IEEE Transactions on Power Electronics Second Place Prize Paper Award, Japan Nikkei Electronics Power Electronics Award in 2021, the Best Paper Award in the 2009 IEEE International Conference on Power Electronics and Drive Systems (PEDS), and the Best Paper Presentation Award in 2012 Annual Conference of the IEEE Industrial Electronics Society (IECON). He serves as an Associate Editor for IEEE TRANSACTIONS ON POWER ELECTRONICS since 2018, and the Chairperson of the semiconductor power converter sector in The Institute of Electrical Engineering of Japan (IEEJ) Transactions on Industry Applications in 2023. He was also the Chairperson of the IEEJ Investing Research & Development Committee on High-Frequency Switching Power Converters and Applied Power Supplies in 2019–2023. He is a Senior Member of IEEJ, and a Member of The Institute of Electronics, Information and Communication Engineers (IEICE) and the Japan Institute of Power Electronics (JIPE).



Ching-Ming Lai (Senior Member, IEEE) received the Ph.D. degree in electrical engineering from National Tsing Hua University, Hsinchu, Taiwan, in 2010.

From 2009 to 2012, he was a Senior Research and Development Engineer with Lite-On Technology Corporation, Taiwan. From 2014 to 2019, he was a Faculty Member with the Department of Vehicle Engineering, National Taipei University of Technology, Taipei, Taiwan. Since 2019, he has been with the Department of Electrical Engineering, National Chung

Hsing University (NCHU), Taichung, Taiwan. He is currently the Professor and the Director of the Intelligent Electric Vehicle and Green Energy Center, NCHU. From February to August 2023, he was a Research Professor with Kobe University, Kobe, Japan. His research interests include electric vehicles (EVs), power electronics, green energy technologies, and intelligent transportation.

Dr. Lai was the recipient of the 2008 Young Author's Award for Practical Application from the Society of Instrument and Control Engineers (SICE), Japan, the Best Paper Award at the 2013 IEEE International Conference on Power Electronics and Drive Systems (PEDS), the Dr. Shechtman Youth Researcher Award from Taipei Tech (2018), the Outstanding Youth Electrical Engineer Award from the Chinese Institute of Electrical Engineering (2018), the Outstanding Education Achievement Award from SAE-Taipei (2019), the Outstanding Youth Control Engineer Award from the Chinese Automatic Control Society (2019), the Outstanding Youth Engineer Award from the Chinese Institute of Engineers-Taichung Chapter (2020), the NCHU Outstanding Industry-Academia Collaboration Award (2021–2023), and the Ta-You Wu Memorial Award from National Science and Technology, Taiwan, in 2023. In addition, according to Elsevier, he was listed in the World's Top 2 of Scientists (Field: Energy) by field in 2021, 2022, and 2023. He was the Co-Chair of IEEE IFEEC-2021, the Tutorial Chair of IEEE IFEEC-2021, IEEE WiPDA-2019, and IEEE IFEEC-2015. He has been serving as an Editor for the IEEE TRANSACTIONS ON VEHICULAR TECHNOLOGY, since 2017, and an Associate Editor for *IEEE Access*, since 2021. He is Fellow of IET and Fellow of the Australian Institute of Energy.